A NUMERICAL DESCRIPTION OF NITROGEN DIFFUSION IN TITANIUM AT ELEVATED TEMPERATURES

by

Daniel Hawker

B.A., Dublin University, 2018

A THESIS SUBMITTED IN PARTIAL FULFILLMENT OF

THE REQUIREMENTS FOR THE DEGREE OF

MASTER OF APPLIED SCIENCE

in

THE FACULTY OF GRADUATE AND POSTDOCTORAL STUDIES

(Materials Engineering)

THE UNIVERSITY OF BRITISH COLUMBIA

(Vancouver)

July 2021

The following individuals certify that they have read, and recommend to the Faculty of Graduate and Postdoctoral Studies for acceptance, the thesis entitled:

A numerical description of nitrogen transport in titanium at elevated temperatures

submitted by   Daniel Hawker   in partial fulfillment of the requirements for the degree of   Master of Applied Science
in   Materials Engineering

Examining Committee:

Steven Cockcroft, Materials Engineering, UBC

Supervisor

David Dixon, Materials Engineering, UBC

Supervisory Committee Member

Daan Maijer, Materials Engineering, UBC

Supervisory Committee Member

Abstract

As part of a program to understand the dissolution of nitrogen-rich titanium solids in liquid titanium, a numerical study of nitrogen diffusion in titanium at elevated temperatures has been carried out. A Landau transformation was applied to the equations governing nitrogen diffusion which were used as the basis for the numerical models developed in this study.

To begin a numerical model describing the nitriding of commercially pure titanium was developed. The numerical model was used initially to simulate nitrogen diffusion in a planar geometry and the predicted nitrogen concentration profiles and displacement of *Ti-N* phase boundaries showed good agreement with analytically derived solutions. The numerical model was then used to simulate nitrogen transport in commercially pure titanium cylinders. The model results were shown to be sensitive to the diffusion coefficients of *Ti-N* phases present in the system. Based on a sensitivity analysis, diffusion coefficients at 1650 °C of 4.3×10^{-11} m$^2 \cdot$s^{-1}, 1.6×10^{-11} m$^2 \cdot$s^{-1} and 1.7×10^{-12} m$^2 \cdot$s^{-1} for β-*Ti*, *α-Ti* and *TiN* phases, respectively, were back calculated using the model. The model predictions, using the new diffusion coefficients, showed good agreement with previously published data in terms of both the nitrogen concentration profiles and displacements of *Ti-N* phase boundaries under the conditions examined in the study. The comparison indicates the model framework is capable of accurately approximating the diffusion of nitrogen in titanium at elevated temperatures.

In work that followed, the model framework was used to develop an improved numerical model for describing the dissolution of *Ti-N* particles in liquid titanium. The results of the improved methodology have been compared to a second finite-difference based model formulated using the conventional approach for interface motion. The improved approach accurately accounts for conservation of nitrogen associated with interface motion and hence has the potential to predict particle dissolution times more accurately in commercial melt refining operations.

Lay Summary

Owing to its material properties, titanium and its alloys are used in the construction of aircraft frames and engines. However, the presence of defects can cause premature failure of the components and have catastrophic consequences. As an example, the presence of one of these defects led to component failure and the crash landing of United flight 232, in 1989. As part of a program to reduce defect occurrence in titanium components, a numerical model has been developed, which describes the process for removal of one type of defect during processing of titanium in the liquid state. The results show that this model can more accurately describe the removal process than previously developed models.

Preface

A significant amount of the work from this research program has been published in a peer-reviewed journal paper, which has been accepted subject to minor revisions at the time of writing this preface (see reference below). This paper embodies Chapter 4, which includes development of the numerical model, its verification against an analytical solution and it application to an example experiment taken from the literature involving nitriding of titanium rods. The contents of Chapter 5 will be submitted shortly for review as a second journal paper.

1) Daniel Hawker, Chris D. Lane, Steve L. Cockcroft, Daan M. Maijer. Numerical Modeling of the Diffusional Transport of Nitrogen in Multi-Phase Solid Titanium and its Application to Determine Diffusion Coefficients. Journal of Materials Research and Technology. Elsevier, 2021.

My contribution was to develop the various forms of the numerical model, verify it using various approaches and apply it to simulate the dissolution of *Ti-N* particles. This last step included assessing the merits of the model in relation to previously published work and also conducting a sensitivity analysis to determine the key model inputs and process parameters having the largest effect on dissolution rates.

Throughout the course of this program, Professor Steve Cockcroft, my supervisor, provided on-going support in the form of advice on all aspects of my M.A.Sc. program. All the secondary authors listed on the paper identified above, provided editorial feedback during the preparation of the manuscripts for publication.

Table of Contents

List of Tables

List of Figures

List of Symbols

Symbol	Description	Unit
b_s	Interface rate constant of interface s	$mm \cdot s^{-0.5}$
c	Nitrogen concentration, $c(r, t)$,	$kg \cdot m^{-3}$
c_i^+	Upper limit for nitrogen concentration in phase i	wt. %
c_i^-	Lower limit for nitrogen concentration in phase i	wt. %
c_0	Initial concentration	wt. %
c_S	Surface concentration	wt. %
D_i	Diffusion coefficient in phase i, $D_i(c(r, t))$	$m^2 \cdot s^{-1}$
D_0	Maximum diffusion coefficient at infinite temperature	$m^2 \cdot s^{-1}$
d_p	Particle diameter	mm
$DT_{BaseCase}$	Time taken for complete dissolution of the simulated base case particle	s
$DT_{TestCase}$	Time taken for complete dissolution to of the simulated test case particle	s
k	Mass transfer coefficient	$m \cdot s^{-1}$
Q	Activation energy	$J \cdot mol^{-1}$
r	Position	mm
R	Universal gas constant, 8.314	$J \cdot mol^{-1} \cdot K^{-1}$
Re	Reynolds Number	
s_1	Position of the β/α interface, $s_1(t)$	mm
s_2	Position of the α/TiN interface (for the nitriding model), $s_2(t)$ Position of the β/Ti_{Liq} interface (for the dissolution model), $s_2(t)$	mm
S	Surface position	mm
Sc	Schmidt Number	
Sh	Sherwood Number	
t	Time	s

T	Temperature	K
u, v and w	Positional variable after Landau transformations	
V_{rel}	Slip velocity	$mm \cdot s^{-1}$
wt. %	Weight percent	
λ	Geometric parameter (1, 2 or 3 for planar, cylindrical or spherical)	
μ	Viscosity	$kg \cdot m^{-1} \cdot s^{-1}$
ρ	Density	$kg \cdot m^{-3}$

Subscripts

Subscript	Description
β	β-Ti phase
α	α-Ti phase
Liq	Liquid titanium
TiN	Titanium-nitride
$\beta\alpha$	Phase boundary between β-Ti and α-Ti phases
αTiN	Phase boundary between α-Ti and TiN phases

List of Abbreviations

CFRP	Carbon fibre reinforced polymer
CHM	Cold hearth melting
CP-Ti	Commercially pure titanium
EBCHR	Electron beam cold hearth remelting
Eqs.	Equations
HID	High interstitial defect
N	Nitrogen
PAM	Plasma arc melting
Ti	Titanium
Ti-64	Ti-6wt%Al-4wt%V
Ti-6242	Ti-6wt%Al-2wt%SN-4wt%Zr-2wt%Mo-Si
UTS	Ultimate tensile stress
VAR	Vacuum arc remelting

Acknowledgements

Chapter 1 Introduction

Titanium and its alloys are characterized by properties such as high strength-to-weight ratio, good resistance to corrosive environments and good mechanical properties over a range of temperatures up to ~500℃. Table 1-1 highlights some of the differences in terms of density, mechanical properties, and cost, between a titanium alloy, Ti-6wt%Al-4wt%V (Ti-64), an aluminum alloy, Al-2024, and an iron-based alloy, 304 stainless steel. Owing to its properties, titanium has applications in the medical, marine, automotive, and aerospace industries. However, production costs of titanium are higher than other commonly used structural metals and their alloys. Its use is therefore limited to high performance applications or where life cycle analysis justifies its cost [1].

Table 1-1. The properties at room temperature [2] and price [3] of selected alloys used in the aerospace industry.

Alloy		Density	Yield strength	Ratio of yield	Cost to produce
Base metal	Alloy name	[kg·m^{-3}]	[MPa]	strength to density [MPa]/[kg·m^{-3}]	base metal [US$·kg^{-1}]
Titanium	Ti-64	4,430	825	0.19	12.00
Aluminum	Al-2124	2,770	440	0.16	2.43
Iron	SS-304	7,930	515	0.06	0.22

The aerospace industry is the principal consumer of titanium products. In the United States the aerospace industry accounts for 70-80 % of titanium consumption. The titanium industry's reliance on the aerospace industry was demonstrated during the 1990s when worldwide titanium sponge production mirrored the fluctuating demand for titanium products by aircraft manufacturers [1]. Titanium is used in the manufacture of aircraft frames and engines. Titanium is used in place of aluminum where the operating temperature will exceed 130°C and in place of steel for weight saving purposes [4]. Further, the amount of titanium used during aircraft production is set to increase. Next generation engines are expected to use up to three times more titanium compared with legacy engines resulting in a 46 % increase in titanium demand by engine manufactures by 2030, see Figure 1-1. Additionally, with the aim of making the aircraft more fuel efficient, the next

generation of aircraft structures are shifting to increased use of carbon fibre reinforced polymer (CFRP) composite materials. In step with the increased use CFRP, titanium use is increasing as it is electro-chemically inert when in contact with the CFRP, whereas aluminum is reactive [5]. The manufacture of Airbus S.A.S.'s low fuel consumption aircraft used more than twice as much titanium as the manufacture of conventional aircraft [4].
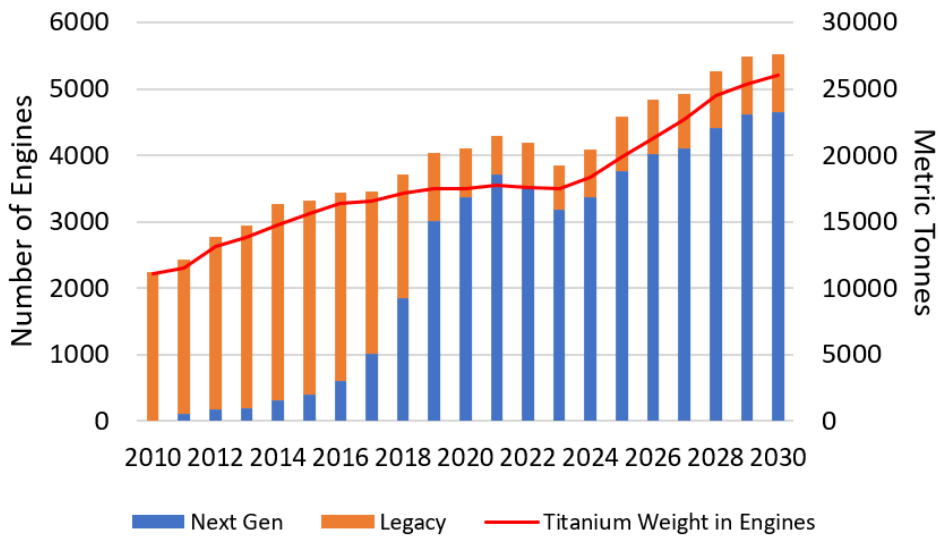
Figure 1-1. On the primary axis, the number of engines produced and predicted to be produced, counting Legacy and Next Generation, is plotted against calendar year. On the secondary axis the metric tonnes of titanium used and predicted to be used in engine construction is plotted [5].

Property consistency and predictability are critical, especially when the material is intended for use in safety-critical components. Undesirable material properties, resulting from incorrect alloy compositions or the presence of defects, can lead to premature component failure and have catastrophic consequences. The production of ingots with consistent quality is not only critical to the end-user of the material, but it is also critical to the producer in order to avoid high scrap rates and keep internal costs at a minimum [6]

Production of titanium ingots occurs in two stages: extraction and consolidation. The following section summarizes the production process of titanium and discusses the role of melt-refining processes in composition control and defect removal during ingot production.

1.1   Titanium production

1.1.1   Titanium extraction

Metallic titanium is extracted from titanium rich ores, such as rutile (TiO_2) or ilmenite ($FeTiO_3$). The process involves passing chlorine gas through titanium ore to form titanium tetrachloride and carbon monoxide as per the overall reaction shown in Eq. 1.1.

$$TiO_2(s) + 2Cl_2(g) + 2C(s) \rightarrow TiCl_4(l) + 2CO(g) \qquad (1.1)$$
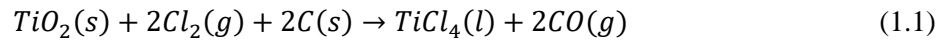
The titanium tetrachloride is then purified by distillation.

The purified titanium tetrachloride is introduced slowly into a large steel vessel with a reducing agent, molten magnesium, in a batch-type process. The process takes tens of hours to complete and is known commercially as the Kroll process. The overall reaction is shown in Eq. 1.2. The Kroll process was developed in 1932 and is still used in the industrial production of titanium. The reaction products at operating temperatures are liquid magnesium chloride and solid metallic titanium. The metallic titanium is known as titanium sponge, as it forms as a porous solid with a sponge like appearance.

$$TiCl_4(g) + 2Mg(l) \rightarrow Ti(s) + 2MgCl_2(l) \qquad (1.2)$$
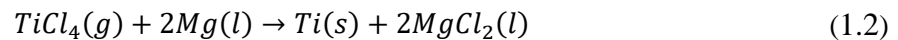
Prior to extraction from the Kroll reactor, the titanium sponge mass is purified using a vacuum distillation process to remove any residual $MgCl_2$ retained within the sponge. The mass of titanium sponge is then extracted from the Kroll reactor and crushed to produce granules of metallic sponge as seen in Figure 1-2. Strict crushing methods are observed to avoid fires that may contaminate the sponge with oxygen or nitrogen that can later result in melt related defects.

Granules of metallic sponge intended for high performance applications, such as aeroengine components, have strict size specification (length < 1 cm), sponge intended for non-safety critical components allow coarser granules (length < 2.5 cm). This practice is designed to ensure that any granules contaminated with nitrogen or oxygen can be removed during the various melt-refining processes that are used to consolidate the sponge into primary ingot.

Figure 1-2. Titanium sponge granules courtesy of TIMET.

1.1.2 Melting/consolidation processes

The melt/consolidation processing of titanium refers to the methods used to produce primary ingots. These ingots may either be used to produce mill products or be remelted for foundry applications. The process involves melting feedstock, composed of one or a combination of virgin metallic sponge and scrap (also called revert), followed by solidification into a wide range of different formats. For the ingots intended for critical applications, the melt/consolidation process must produce a homogeneous, high quality and defect free ingot. The need to ensure the elimination of melt related defects from the final product means that elaborate steps are taken to inspect and handle the feed material, to implement and control the melting processes, and to inspect the final product.

Focusing on the melt/consolidation processes, these processes must be designed and operated to avoid the occurrence of the five main melt related defects. Table 1-2 summaries and lists the potential causes of the melt related defects. Additionally, the reactivity of titanium in the molten state means that the melt processes must be carried out under vacuum or inert gas conditions. Commercially, high-grade titanium ingots are melted and consolidated using one or a combination of vacuum arc remelting (VAR), electron beam cold hearth melting (EBCHM), and plasma arc melting (PAM).

Table 1-2. A summary of the possible causes of the five main melt related defects [1].

Defect Type	Possible Causes
High Interstitial Defect (HID) Type 1 ("Hard alpha")	Sponge production - Contaminated magnesium reductant - Fires during handling or shearing First melt electrode production - Fires during compaction - Improperly conditioned scrap - Contaminated master alloy - Contamination during welding Melting and remelting - Small water leak - Air leak - Aggressive grinding during ingot conditioning
High Density Inclusions (HDIs)	Scrap additions - Tungsten welding electrodes - Tool bits mixed into turnings
Beta Flecks	Melting segregation Conversion too close to α-Ti/β-Ti transus temperature (including adiabatic heating effects)
Type II (Alpha Stabilized)	Improper final melt phase (excessive pipe formation) Improper ingot top removal Al-rich "drop-ins" during EBM
Voids	Incorporation of shrinkage pipe during conversion Improper conversion practice

Vacuum arc remelting – The VAR process, shown schematically in Figure 1-3, was the first process used to produce large titanium ingots on an industrial scale. VAR has been used by industrial producers since titanium became a commercial product in the 1950s. The VAR process can produce ingots as large as 100 cm diameter and weighting up to 15,000 kg [1]. The process can produce commercially pure titanium (CP-Ti) and a wide range of alloys including the dominant structural alloy Ti-64. Alloys that are prone to alloy segregation are typically produced with smaller diameters to prevent the formation of beta fleck and type II defects.
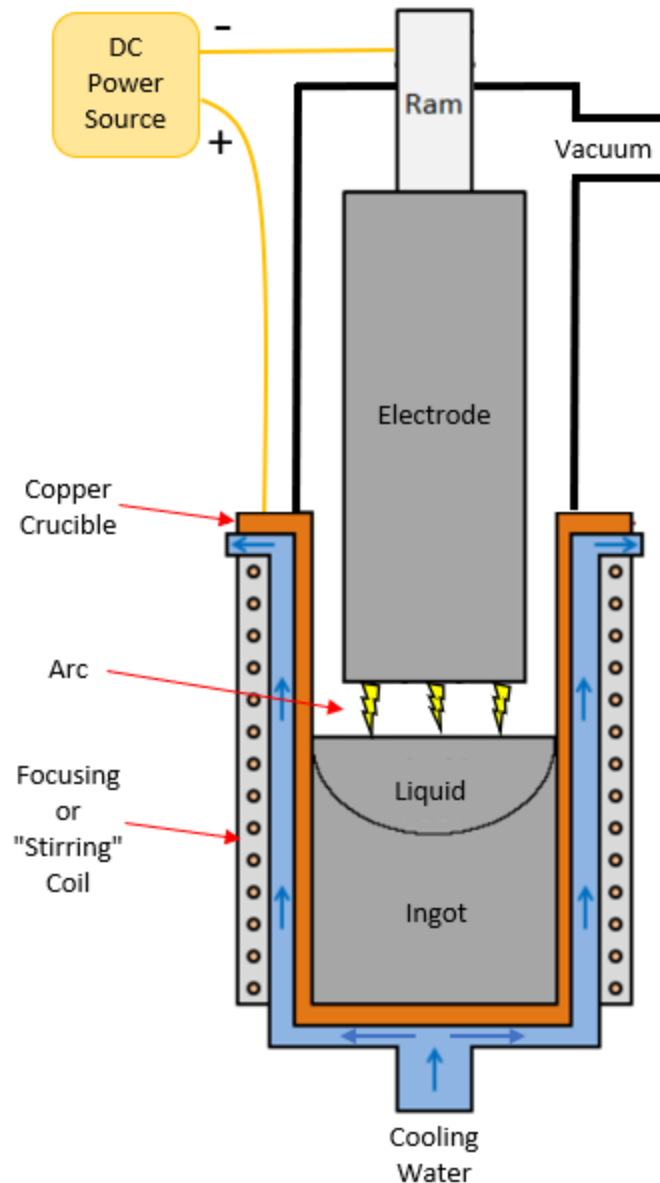
Figure 1-3. Schematic illustration of the VAR process.

To start the VAR process titanium sponge and alloying elements are blended and then hydraulically pressed to produce blocks (briquettes). A first-melt electrode is produced by welding the blocks together in an inert gas welding chamber. Due to economic advantages of recycling and reusing titanium scrap, unalloyed grades and non-rotary grade alloys are added to the electrode during welding. Care is taken with regards to the origin and cleanliness of the scrap to prevent the introduction of unwanted elements to the electrode.

Once welded, the electrode is then suspended in a water-cooled copper mould of slightly larger diameter under a vacuum. To begin the melting/remelting process, the electrode is lowered to contact and then initiate an arc with the bottom of the mould. The arc provides the heat to slowly melt and consume the electrode. The molten material forms a molten pool within the copper mould which then solidifies to form the ingot. Once the electrode is fully consumed, the ingot produced from the melt is removed, inverted, and melted again in the VAR furnace. If the material is intended for application in rotary components, the ingot is melted for a third time [6].

Advantages of VAR are that the final ingot has good homogeneity and rates of loss of alloy elements through volatilisation are low. However, during the VAR process, dense inclusions sink to the bottom of the melt pool and remain in the ingot, forming HDIs in the final product. Furthermore, nitrogen and/or oxygen rich inclusions (*Ti-N* and *Ti-O*) inclusions, which form HIDs in the final ingot, may survive the VAR process because they 'short circuit' the melt pool – i.e., the contaminated particles do not spend adequate time the melt pool for complete removal by dissolution to occur.

Cold hearth melting - CHM was first used in the melting of titanium in 1985. The two variants of CHM are PAM and EBCHM. A schematic of commercial-scale EBCHM is shown in Figure 1-4. The melting vessel for both EBCHM and PAM is made from water-cooled copper and is known as a hearth. Due to the high rate of heat extraction from the hearth, a solid layer of titanium forms on the hearth walls and bottom known as a skull. The skull prevents the molten material from reacting with and being contaminated by the hearth material. PAM uses a plasma torch as a heat source and is carried out under an inert gas atmosphere, normally argon or helium. Conversely, EBCHM uses an electron beam as a heat source and must be carried out under vacuum conditions.
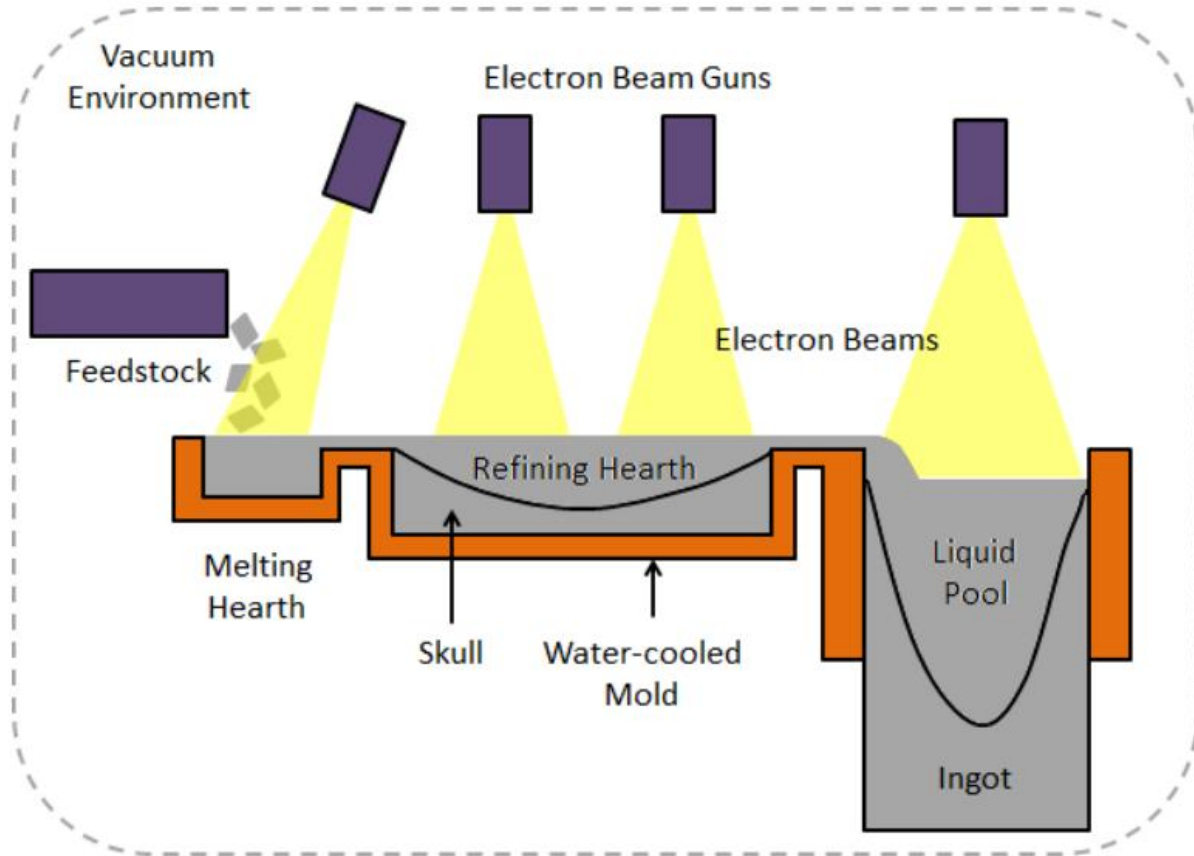
Figure 1-4 An illustration of electron beam melting is shown [7].

Unlike VAR, CHM allows casting of both axisymmetric and non-axisymmetric shapes. This can reduce the cost of subsequent conversion operations depending on the application. The major advantage that CHM offers over VAR is an increased capability of producing ingots free from HDIs and HIDs. The use of titanium scrap can inadvertently introduce denser elements in the form of tungsten carbide tool bits or tungsten welding electrode tips, which may form HDIs in the final ingot. CHM induces gravity separation of dense inclusions in the hearth trapping them in the skull prior to entering the mold and final ingot. Additionally, titanium scrap that has been flame cut or titanium sponge that has been exposed to air at elevated temperatures can lead to the presence of *Ti-N* and / or *Ti-O* inclusions in the melt pool, which may form HIDs in the final ingot. CHM allows for long residence times of these inclusions in the melt pool as they travel the length of the refining hearth(s) allowing for their removal via dissolution. CHM has therefore become a critical technology in the producing of rotor-grade titanium from revert.

Although CHM is an effective method of removing HIDs and HDIs, the process can induce other defects in the final ingot. During EBCHM, high volatilisation rates of alloy elements can occur due to the vacuum environment. In the case of aluminum, the evaporation of aluminium results in deposits forming on the cold walls and roof of the furnace. These deposits can detach and fall back into the melt if they become excessively large resulting in a region enriched in Al that may persist and be present in the ingot if there is not adequate time for melting and homogenization. During PAM there is also the possibility that small inert gas bubbles can form in the melt which can result in pores in the final ingot. As such, ingots produced by both CHM processes are subject to a final VAR process before they can be accepted for use in rotary grade material. This VAR allows for re-homogenisation of Al-rich regions and/or release of trapped bubbles in the ingot.

The application and development of CHM technologies to the melt process has significantly reduced the occurrence of HIDs in titanium ingots. The reported rate of occurrence is now two HIDs per million kilograms produced [1]. However, due to the material's intended application in aircraft manufacture and the potentially fatal consequences of component failure, this level of occurrence is still unacceptable.

To qualify CHM furnaces to produce rotor-grade material, the furnace must pass a seeded trial, in which *Ti-N* inclusions are deliberately added to the melting hearth. If any inclusions are found in the final ingot produced in the seeded trial, then the furnace cannot be approved for ingot production.

Ti-N inclusion removal - The process of removal of HID's in liquid titanium is complex, and although it has been investigated in several studies, there remains a lack of a good quantitative understanding of the process. In the case of *Ti-N* inclusion removal, the process is controlled by the mass transport of nitrogen within the solid and transport of nitrogen at the *S/L* interface to the bulk liquid. Titanium normally has two allotropes, *α-Ti* present at room temperature and *β-Ti* present at temperatures above 882℃ and below the melting point. The presence of a small amounts of nitrogen both increases the temperature range of α-*Ti* stability and significantly raises the liquidus temperature. Mathematically, the dissolution problem therefore falls into the category of a classic Stefan problem with two moving phase boundaries *α-Ti/β-Ti* and *β–Ti/liquid*, each with

a step change in the nitrogen content at the phase boundary. The focus of this work is on developing a numerical model which approximates the multi-phase transport of nitrogen in solid titanium addressing some of the limitations in the previously published numerical models.

Chapter 2 Literature review

2.1   Characterisation of high interstitial defects

HIDs result in a hard and brittle region in titanium castings that can potentially act as a fatigue crack initiation site under cyclical loading conditions. Their presence in safety critical components is unacceptable because they can cause the component to fail prematurely. In 1989, the presence of a HID in the General Electric fan disk of United Airlines Flight 232 led to loss of many flight controls and a crash landing in Sioux City, Iowa. Many examples of HIDs have been studied by industrial producers. The results from these studies were summarised by Mitchell [8], who described the form of the defect as follows:

- The defects may be characterized as alpha-stabilized regions in the final casting caused by the presence of nitrogen alone, in the concentration range up to 10 wt.%, or by a combination of nitrogen and oxygen, with the maximum oxygen concentration measuring 5 wt.%.
- Porosity and cracks may or may not be present in the defect volume.
- The concentration of the alloy elements in the defect ranged from zero to the base alloy concentration.
- HIDs have been found in ingots made from sponge, scrap, and a combination of the two.
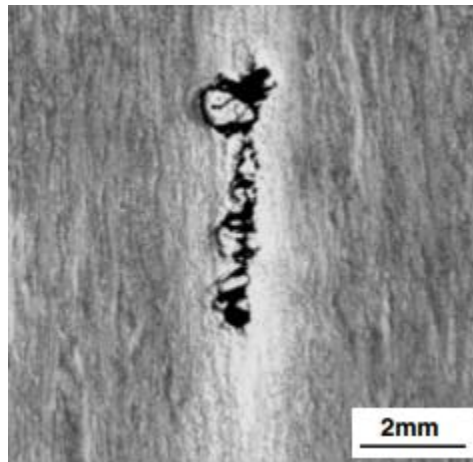
Figure 2-1. HID in a Ti64 forging. Reprinted by permission from Springer Nature: Springer eBook [1].

Figure 2-1 is an example of a HID in a titanium forging. They are formed in titanium ingots and billets when *Ti-N* and/or *Ti-O* inclusions survive the melt-refining process(es). The potential

sources of *Ti-N* and/or *Ti-O* inclusions were summarised in Table 1-2. Like HIDs, the form, the nitrogen concentration, and the nitrogen distribution of the inclusions entering the melt-refining process vary significantly. Inclusions can be porous, if they originated from sponge, or nonporous, if they originated from scrap. Further, Henry et al. [9] reported uneven nitrogen distributions in *Ti-N* inclusions, which were formed by exposing titanium sponge granules to nitrogen concentrations consistent with levels that occur via air leakages and contaminated magnesium during industrial production.

The titanium industry attempts to limit the occurrence of HIDs in safety critical components through strict control of feedstock material used during melt-refining, screening of ingots and billets, and specially designed melt-refining practices. Careful control of input materials used in sponge production, and care when handling of sponge and scrap significantly reduces nitrogen and oxygen contamination.

After the melt-refining process(es), the primary ingots are screened for shrinkage related voids using ultrasonic inspection. They are then deformed to a specified amount and re-inspected. If above a certain size threshold, the ultrasonic inspection can detect the void typically created by a strain incompatibility between the ridged HID and the metal matrix. In practice, signal attenuation, caused by *β-Ti* microstructures, and signal reflection, caused by the elastic anisotropy of *α-Ti* microstructures, reduces the efficacy of HID detection. Deciphering if a reflected signal is caused by the orientation of titanium microstructures or a HID is challenging, particularly for HIDs that are not extensively porous or cracked. As a result, HIDs, large enough to cause premature failure of components, can go undetected during ultrasonic inspection. The titanium industry has, therefore, adopted the philosophy that the melt-refining processes must guarantee inclusion removal for rotor-grade titanium production [1].

2.2 Experimental studies on *Ti-N* inclusion removal in liquid melt pools

Before discussing the exact mechanisms of *Ti-N* inclusion removal during industrial melt processing it is beneficial to distinguish between the thermodynamic processes of melting and dissolution. The process of melting occurs when an inclusion becomes immersed in a liquid where the temperature of the bulk liquid exceeds the melting/liquidus temperature of the inclusion. Thermal energy will be transferred from the liquid to the inclusion and, providing the liquid

contains enough thermal energy, the temperature of the inclusion will increase to the point that it is thermodynamically favourable to transform from a solid to a liquid. Conversely, in dissolution, the composition of the inclusion results in it having a melting point/liquidus temperature above the bulk temperature of the liquid. The transformation from solid to liquid occurs when the composition at the *S/L* interface is altered sufficiently to reduce the melting/liquidus temperature to bulk liquid temperature. Thus, the transformation from solid to liquid state is controlled by mass transfer, or a combination of mass and heat transfer between the liquid and the inclusion. The kinetics of melting are hence governed by the rate of heat transfer while the kinetics of dissolution are governed by the rate of mass transfer or a combination of mass and heat transfer.

Figure 2-2 shows the binary titanium-nitrogen phase diagram. The liquidus temperature of *Ti-N* inclusions increases significantly with nitrogen concentration. Given the temperatures vary from 1668-2020°C in standard melt refining processes, the maximum temperature a *Ti-N* inclusion will experience may lie below its liquidus temperature, even for inclusions with relatively low nitrogen concentrations (> 2 wt. % N). The transport of nitrogen from the inclusion to the surrounding melt pool therefore plays an important role in *Ti-N* inclusion removal.

Comparison of the thermal and mass diffusivities for the *Ti-N* system demonstrate that mass is transferred much slower than heat (∼1000 times slower). Therefore, the transport of nitrogen from the inclusion to the surrounding melt pool is the rate-defining step in the dissolution process. The transfer of nitrogen occurs in the solid inclusion via diffusion, and in the liquid boundary layer surrounding the inclusion via convection. *Note: convection is a combination of diffusion and advection.*
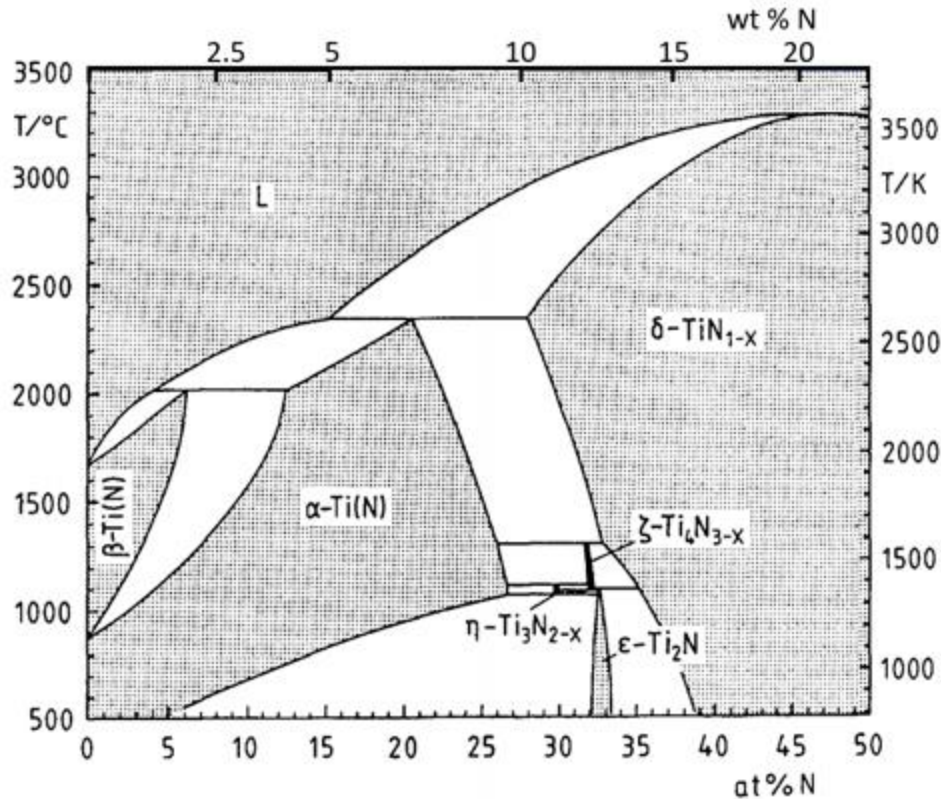
Figure 2-2. Complete equilibrium phase-diagram of the *Ti-N* system. Reprinted by permission from Elsevier Science and Technology. [10].

Experimental Studies – Studies have investigated the dissolution of *Ti-N* inclusions using small scale representations of industrial melt refining processes. *Note: The term 'Ti-N inclusion' is used as a general term to refer to any titanium sample that contains nitrogen.* Figure 2-3 shows a typical experimental set up where a nitrogen enriched specimen is immersed in a titanium or titanium alloy melt pool. Setups akin to Figure 2-3 have most commonly been used to investigate the dissolution of non-porous titanium samples with uniform nitrogen concentrations, known as synthetic inclusions [11][12][13]. The dissolution behavior of sponge particles with uniform [14][15] and non-uniform [16] nitrogen concentrations have also been investigated. One study compared the dissolution behavior of synthetic inclusions and compacted titanium sponge rods [17].
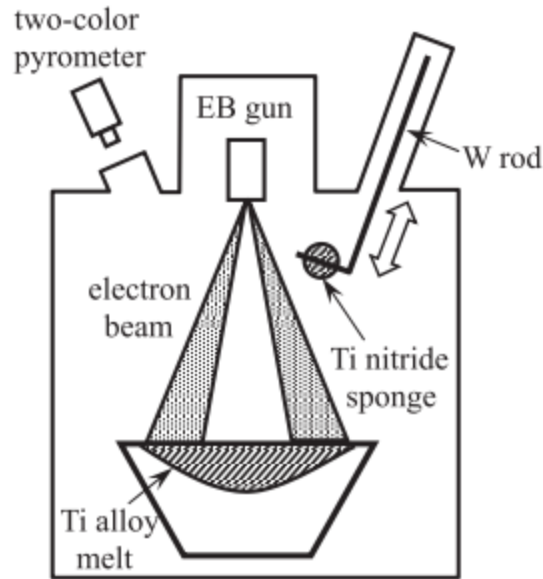
Figure 2-3. A schematic of a typical experimental set up to investigate the dissolution of nitrided titanium sponge and synthetic inclusions [15].

Microstructural Observations - Bewlay et al. [16] immersed non-porous titanium nitride (*TiN*) rods with a uniform nitrogen concentration of 15 wt.% in a Ti-6wt%Al-2wt%SN-4wt%Zr-2wt%Mo-Si (Ti-6242) melt pool at 1725 ℃ for up to 100 minutes. After quenching and sectioning the rods, a microstructural analysis showed the initial *TiN* rods were surrounded by successive layers of *α-Ti* phase and acicular *α-Ti* phase. Figure 2-4 demonstrates that identical phase nucleation was also observed by Bellot et al. [14] when immersing nonporous plates with a uniform nitrogen concentration of 5 wt.% in a CP-Ti melt pool. In both studies, the lower and upper nitrogen concentrations reported in *α-Ti* and acicular *α-Ti* phases approximately coincide with the nitrogen concentration limits predicted by the *Ti-N* phase diagram for *α-Ti* and β-*Ti* phases at 1725 ℃. Bewlay et al. [16] confirmed that the acicular alpha phase was solid at the time of dissolution by doping the melt pool with iron for 15 s at the end of a dissolution experiment. *Note: The melting point of iron is 1538°C. Iron will therefore melt in liquid titanium, sink as it is denser, and accumulate at the S/L phase boundaries. Application of a chemical etch will allow the extent of the melt pool to be delineated as titanium and iron will react differently to the etchant.* The results indicate that the acicular *α-Ti* phase was β-*Ti* phase during the dissolution process.

The formation of *α-Ti* and *β-Ti* phases during the dissolution of *TiN* rods is a result of the nitrogen diffusion in the rod. Each phase has a thermodynamic stability range that is a function of temperature, pressure, and nitrogen concentration. The diffusion of nitrogen reduces the nitrogen concentration close to the surface of the rod where it becomes thermodynamically favorable for the new phases, *α-Ti* and then β-*Ti*, to nucleate. The newly formed phase interfaces, *TiN*/*α-Ti*, *α-Ti*/β-*Ti*, and β-*Ti*/Ti$_{Liq}$, propagate towards the center of the rod until complete dissolution of the rod occurs. *Note: the β-Ti / Ti$_{Liq}$ interface may initially propagate outwards as the nitrogen flux freezes the liquid adjacent to the particle surface.*
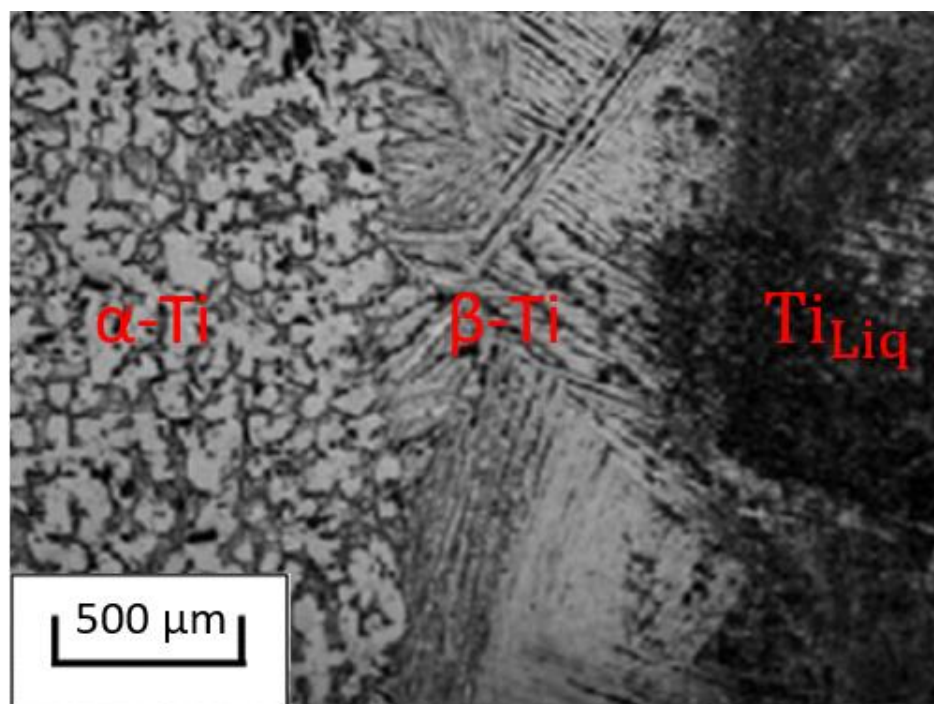
Figure 2-4. The microstructure of a partially dissolved synthetic inclusion measured at room temperature. The labels show the phases that are assumed to be present at the time of dissolution. Copyright © 2010 by The Minerals, Metals & Materials Society and ASM International. Used with permission [18].

Microstructural analysis has also been conducted on partially dissolved titanium sponge particles with uniform nitrogen concentrations [14][15] and non-uniform nitrogen concentrations [16]. The studies report continuous layers of *α-Ti* phase and acicular *α-Ti* phase surrounding a particle center composed of *TiN* phase. The relative sizes of the surrounding layers were reported

16

to be approximately 10 μm for the *α-Ti* phase and between 100-300 μm for the acicular *α-Ti* phase. The width of the acicular *α-Ti* phase decreased for increased fluid flows in the melt pools. The microstructural observations are consistent with those reported during the dissolution of synthetic inclusions.
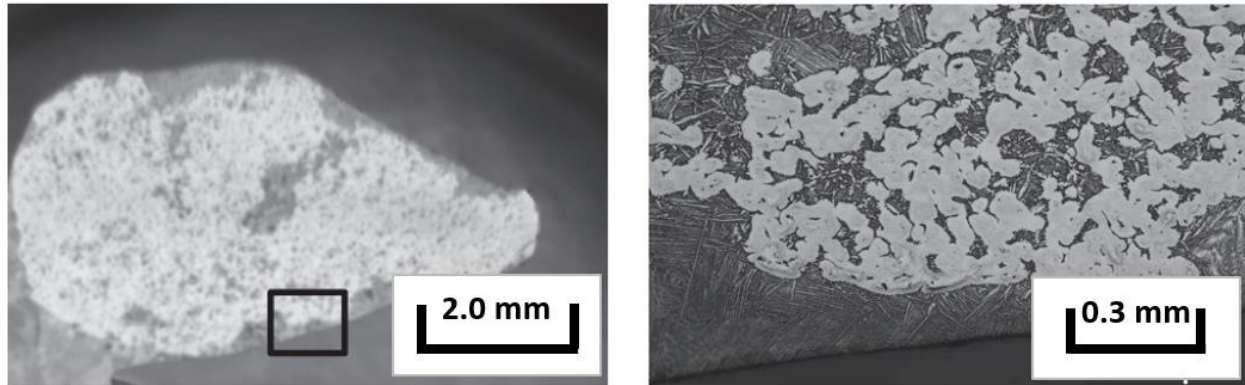
Figure 2-5. Titanium nitride sponge after immersion into titanium alloy melt [15].

Microstructural analysis of the initially porous sponge particles was also conducted on the permeation zones. *Note: the permeation zone is the region that was initially porous but was filled with the permeating liquid.* Bewlay et al. [16] commented that the microstructures, *TiN*, *α-Ti*, and acicular *α-Ti* phases, formed at the interface between the sponge fibers and the permeation zone are the same, but on a smaller scale, as the microstructures formed on the outside of the particle. Figure 2-5 shows the microstructure of a partially dissolved nitrided sponge particle, the needle like microstructure of the acicular *α-Ti* phase can be clearly observed both surrounding the particle and in the permeation zones.

Dissolution Kinetics – Reddy [12] studied the dissolution rate of uniformly nitrided titanium rods by submerging the rods in CP-Ti melt pools. The study varied the velocity of the fluid flow in the melt pool via stirring and found that the dissolution rate of the rods increased with degree of stirring. A study conducted by Schwartz [11] confirmed Reddy's findings when he recorded dissolutions rates ten times greater for stirred melt pools than rates recorded in unstirred melt pools. Similar studies have investigated the effect of melt pool temperature on the dissolution rates of synthetic inclusions [13]. Figure 2-6 demonstrates that dissolution rates of synthetic inclusions

increase exponentially with increases in temperature. The increase in dissolution rates has two root causes. Firstly, increases in temperature may lead to an increase in the buoyancy and Marangoni driven flow in the bath. The increased flow reduces the size of the boundary layer surrounding the inclusion which in turn increases the convective nitrogen transfer from the inclusion to the melt pool. Secondly, the diffusion coefficients of nitrogen in solid titanium also increase exponentially with temperature, leading to increased nitrogen diffusion rates within the solids [19].
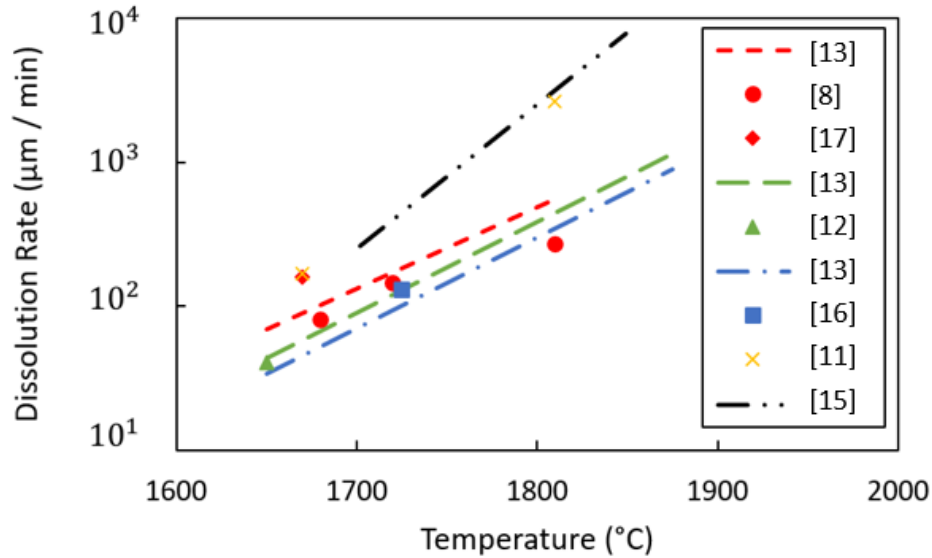
Figure 2-6. Summary of the dissolution rates as a function of temperature for *TiN* synthetic inclusions in CP-Ti (red), Ti-64 (green) and Ti6242 (blue) melt pools; and of *TiN* sponge in an unknown titanium alloy (black) melt pool.

The studies demonstrate that dissolution kinetics of synthetic inclusions vary significantly with both the temperature and fluid flow of the melt pool surrounding the inclusions. Mitchell [8] postulated that temperature and fluid flow gradients within melt pools result in the dissolution rates of inclusions varying with position. Mizukami et al. [15] proposed this as a reason for measuring higher dissolution rates than those found in previous studies, see Figure 2-6. Mizukami et al. suggested that higher dissolution rates were because the nitrided sponge particles were positioned close to the surface of the melt pool, where the fluid flow and temperature of the melt pool were at their maximum values. It is unclear if the variance in dissolution rates was solely a result of the particle being close to the surface of the melt pool, as suggested by Mizukami et al., or if the dissolution kinetics of nitrided sponge particles and synthetic inclusions differ. Van den Avyle et

al. [17] compared the dissolution rates of nitrided sponge rods and synthetic rods. The change in length of each rod was measured after partial dissolution in a CP-Ti melt pool. Figure 2-7 shows that the dissolution rates of the nitrided sponge rods were at least 50% greater than those measured for solid *TiN* rods. Conversely, Bewlay et al. [16] reported that the dissolution rate of *TiN* sponge and *TiN* solid rods were similar. However, the comparison by Bewlay et al. was not quantitative, and there were difficulties in measuring the exact dissolution rate for the sponge due to its irregular shape.
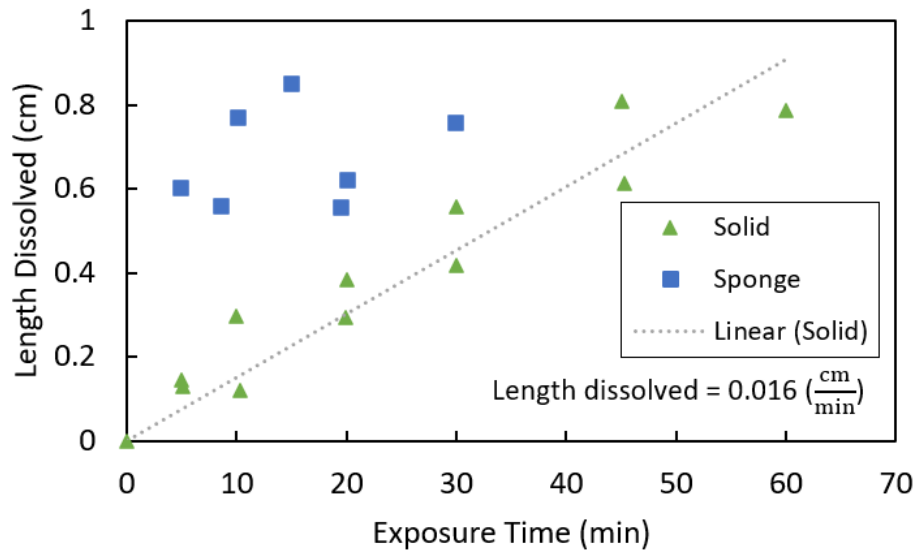
Figure 2-7. Dissolution of solid *TiN* rods and 15 wt. % nitrogen titanium sponge rods in an EB furnace hearth [17].

Liquid Penetration Behavior in Porous Ti-Sponge – All studies examining the dissolution of porous sponge report penetration of the melt pool liquid into the pores of the sponge. The penetration of the liquid into the pores densified the particles, reducing and in some incidences eliminating porosity of the particle. Bellot et al. [14] reported residual porosity values varying from 1-23 % while Van de Avyle et al. [17] stated that the residual porosity was not consistent between samples. Bellot et al. hypothesized that the residual porosity was a result of either a high residual gas pressure in the pores preventing liquid permeation, or that the liquid permeating into the pores solidified, because of nitrogen diffusion from the sponge fibers, preventing complete permeation.

Bellot et al. reported that the amount of nitrogen that diffused into the permeation zone was different for CP-Ti and Ti-6242 melt pools. The permeation zone contained on average 6 wt. % nitrogen when the sponge particle was immersed in a CP-Ti melt pool for 80 s but only 1 wt. % nitrogen when the sponge particle was immersed in Ti-6242 melt pool for 120 s. Given that Bellot et al. measured lower nitrogen diffusion rates in the permeation zones in a Ti-6242 melt pool than a CP-Ti melt pool and the shrinkage of nitrided particles is partially controlled by the diffusion of nitrogen, it is possible that nitrided sponge particles may dissolve slower in Ti-6242 melt pools.

2.3   Computer models of *Ti-N* inclusion removal

Synthetic Inclusions - Bellot et al. [14] attempted to describe the dissolution of synthetic inclusions from a theoretical viewpoint. The study numerically models the dissolution of a plate and sphere with nitrogen concentrations of 5 wt. % in a liquid titanium melt pool. The model assumes that the dissolution of the particle is governed by the diffusional transport of nitrogen in α-*Ti* and β-*Ti* solid phases, and the convective transport of nitrogen at the solid / liquid interface. Additionally, the models assume the particles are isothermal, the nitrogen transport is one-dimensional, and the density of the particles are constant. The model output approximates the evolution of the nitrogen concentration profile in α-*Ti* and β-*Ti* solid phases, and the locations of the α-*Ti* / β-*Ti* and β-*Ti* / Ti_{Liq} phase boundaries.

Figure 2-8 shows the comparison of the numeric model results to an experimentally derived nitrogen concentration profile. The model appears to qualitatively predict the profile of nitrogen in the various phases, but quantitative differences are apparent. Experimental data demonstrates that the thermal and fluid flow regimes significantly affect the dissolution kinetics. Inaccurate representation of these conditions may explain the deviation between the numerical and experimental data. Some of the assumptions in formulation of the numerical model may also contribute to the differences observed.
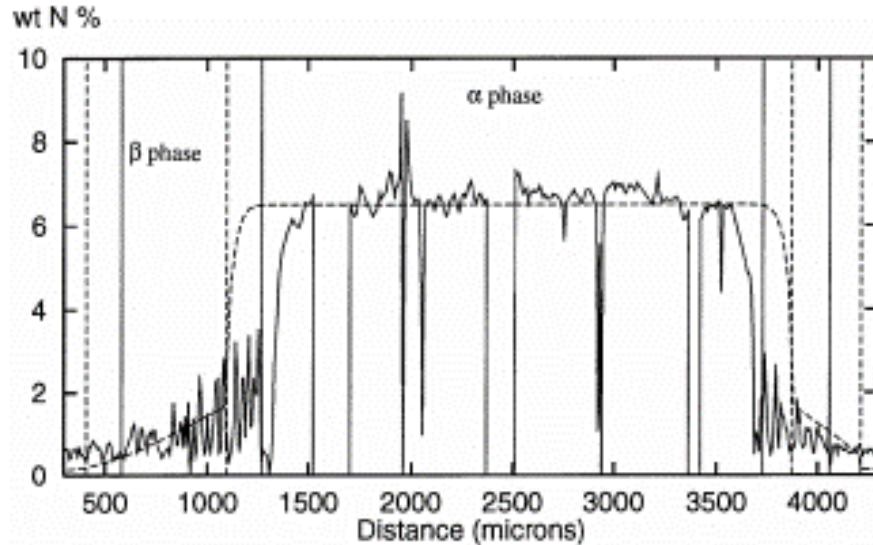
Figure 2-8. Comparison between experimental (continuous line), measured using electron microprobe analysis, and calculated (dotted line) nitrogen profiles. Copyright © 2010 by The Minerals, Metals & Materials Society and ASM International. Used with permission [14].

The dissolution of solid *Ti-N* inclusions is an example of a Stefan problem as the diffusive transport of nitrogen gives rise to moving solid-solid and solid-liquid phase boundaries. For Stefan problems involving diffusive mass transport, Illingworth et al. [20] highlights that numerical errors may arise when coupling Fick's second law, which describes mass diffusion within a given phase, with mass balance equations, which describe the phase interface motions. The errors can result in significant mass loss and inaccurate description of the interface motions.

In numerical models, the moving phase interfaces must be tracked accurately throughout a domain approximated by a finite number of points (nodes). The solution requires solving Fick's second law in the domains associated with the different phases. Studies by Caldwell et al. [21] and Illingworth et al. [20] highlight potential methods to solve Stefan problems numerically. However, it does not appear that any of these approaches were used in the *Ti-N* dissolution model by Bellot et al. [14].

Synthetic Inclusions in CHM - The dissolution model developed by Bellot et al. [14] was used in conjunction with a numerical model of a lab-scale EB-CHM furnace to estimate the survival probabilities of spherical synthetic inclusions [22]. The EB-CHM model was developed by

21

coupling momentum and heat transport equations with the previously developed dissolution model. A similar model was also developed by Van den Avyle et al. [17] but, unlike Bellot et al.'s study [22], the model used dissolution rates from experimental data instead of modelling the process. Both studies assessed the survival probability of inclusions as a function of particle density and initial diameter.

Powell et al. [23] predicted that the residence times of particles varied significantly with particle density and initial diameter, see Figure 2-9. The findings from Powell et al. and Bellot et al. indicate inclusions with large density differences relative to the melt pool (>3%) were unlikely to survive CHM. Denser inclusions were predicted to settle rapidly to the bottom of the melt pool, becoming embedded in the skull and prevented from passing through the hearth. Less dense inclusions were predicted to float to the melt pool surface where they were likely to dissociate due to exposure to the heat source or become embedded in the skull. The models therefore predict that inclusions in a narrow density range around neutral buoyancy were most likely to survive CHM. The neutrally buoyant particles were predicted to remain suspended until they dissolve or pass through the hearth.
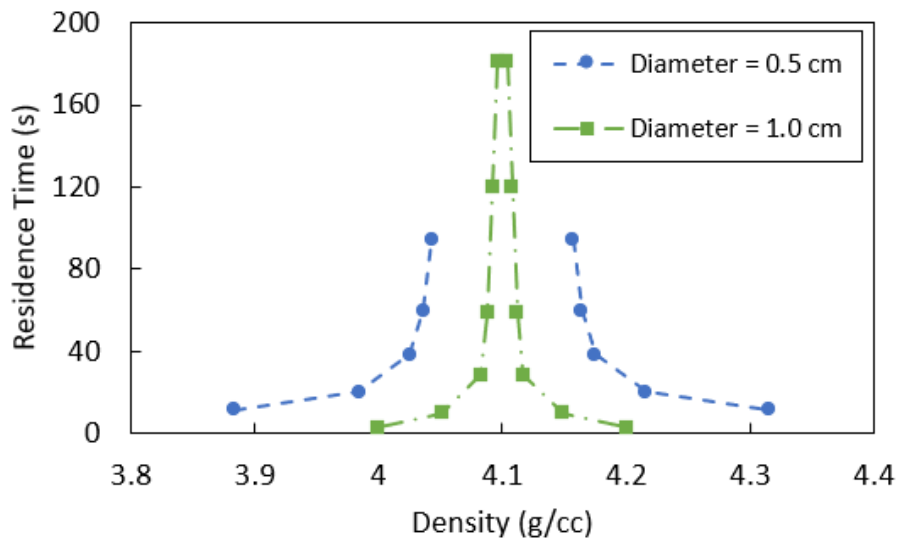
Figure 2-9. Model predicting the residence times of a spherical synthetic particles in CHM as a function of particle density. Dense particles settled rapidly while less dense particles quickly floated to the surface of the melt pool [23].

Powell et al. [23] noted that the hearth-melting process can be designed to provide sufficient residence time to ensure the dissolution of particles up to a given size, and care must be taken to ensure that the inclusions do not experience a direct rapid flow path through the hearth, known as short circuiting. Bellot et al. [22] showed that the flow paths of the inclusions depend on the pattern traced by the heat source of the hearth, the electron beam or plasma arc. To ensure complete dissolution of the inclusions, the pattern of the heat source should be optimized to provide long residence times. However, during the production of titanium alloys containing aluminum, the volatilization of the aluminum increases with increasing residence times, leading to poor chemical homogeneity in the cast products. As such, the pattern traced by the heat source should maximize the residence time for complete dissolution of inclusions while ensuring acceptable chemical homogeneity in the cast products. The models demonstrate that CHM has the capacity to remove most inclusions, but large neutrally buoyant inclusions remain a concern for industrial producers.

Synthetic Inclusions in VAR - A model coupling heat and momentum transport equations with the original dissolution model published by Bellot et al. [14] was developed by Ghazal et al. [18] and used to simulate inclusion dissolution during the VAR process. The melt pool in the VAR furnace solidifies to become a remelt electrode or a primary ingot. As such the removal of *Ti-N* inclusions through density segregation is not possible. All inclusions must be removed through dissolution or exposure to the heat source. The model predicts that only inclusions below a critical size (diameter < 0.3 mm) were likely to be removed through dissolution during a single VAR processing stage. Triple VAR of electrodes could remove inclusions as large as 1 mm in diameter. However, the model predicted that inclusions above 1 mm in diameter would be present in the final ingot.

The model also showed that removal of inclusions (diameter = 1mm) depends on when and where the inclusions were introduced into the melt pool. The trajectory of two inclusions introduced into the melt pool at the same location 10 seconds apart were compared. The inclusions had different trajectories through the melt pool, and the residence times were 12 s and 48 s, respectively. Additionally, the trajectories and subsequent dissolution behaviors of inclusions was shown to vary significantly for inclusions whose densities ranged from 1.00 and 1.03 times the density of the melt pool. Although the model demonstrates that VAR has the capability to remove

some inclusions through dissolution, removal of *Ti-N* inclusions is more likely during CHM owing to the additional benefit of denser inclusion sinking where they are trapped within the skull.

Nitrided Sponge - Only one study could be found that described the dissolution of nitrided titanium sponge from a theoretical viewpoint. Mizukami et al. [15] assumed that titanium sponge was structurally symmetric with a repeating pattern of 50 μm regions of solid titanium and 50 μm regions of liquid titanium. The time for a single 50 μm solid region to completely dissolve was less than 1 second and dissolution of the solid regions was predicted to occur in series, starting with the regions on the outer edge of the particle and dissolving towards the particle's center. The details of how this model was built were not published and the results were not compared to experimental data. It is also unclear how representative this model is of sponge dissolution during CHM and VAR.

No study was found that modeled the dissolution of nitrided titanium sponge in CHM or VAR. Numerical models by Bellot et al. [22], Van den Avyle et al. [17], and Ghazal et al. [18] show that the density of the synthetic inclusions has a significant effect on survival probabilities of the inclusion and other studies found that the density of nitrided sponge evolves during the dissolution process. It can be inferred that a model must precisely predict the density evolution of nitrided sponge to accurately predict the survival probabilities of the particle. No quantitative data could be found on the density evolution of nitrided sponge. More experimental data should be collected on the penetration behavior of liquid titanium into nitrided titanium sponge and subsequent density evolution of *Ti-N* particles.

Numerically modelling the dissolution of *Ti-N* inclusions in liquid titanium is complex as the transport of nitrogen gives rise to *solid/solid* (S/S) and *solid/liquid* (*S/L)* phase boundary motion, which is difficult to simulate accurately leading to mass loss of N. In addition to describing the nitrogen transport within *Ti-N* inclusions, experimental data has shown that the fluid-flow regimes encountered by the particle can significantly alter rates of dissolution. The focus of this work is to apply a new numerical approach that describes nitrogen transport and phase boundary motion in *Ti-N* particles that ensures a minimum mass loss of nitrogen associated with interface motion. As part of the model development strategy, the model formulation is first verified against analytical solutions. Following this, the model is then verified using experimental data derived

from the nitriding of CP titanium rods at 1650ºC, which is a conjugate process to the dissolution of *Ti-N* inclusions – i.e., nitrogen transport is inward. Finally, the model is reformulated using spherical coordinates and used to predict the dissolution time of spherical *Ti-N* particles. In this last phase of the work, the dissolution rates predicted by the new model are compared with the rates predicted from a formulation adopted in the previous work of Bellot et al. [14]. The two approaches are compared in terms of their ability to conserve nitrogen.

Chapter 3 Scope and objectives

HIDs can degrade the fatigue performance of titanium and its alloys and are not acceptable in material for use in rotary grade applications. In conjunction with strict control of feedstock, the industry has adopted the philosophy that the melt-refining processes must guarantee *Ti-N* inclusion removal for rotor-grade titanium production.

Numerical models offer the ability to investigate and improve our understanding of *Ti-N* inclusion removal during the melt-refining processes currently in use commercially. Previous studies have presented numerical models of the dissolution of *Ti-N* inclusions in liquid titanium; however, the models have not been conclusively validate against experimental data. Moreover, the previous approaches may be susceptible to numerical error leading to mass loss of nitrogen associated with phase interface motion in a discretized domain.

3.1 Scope of the research program

The main aim of this program is to develop a finite difference numerical model to describe the transport of nitrogen in titanium at elevated temperatures. As a prelude to developing the dissolution model, a model describing the nitriding of CP-Ti was developed, which is a less complex process. The nitriding process exhibits inward motion of the α/β phase boundary, which is opposite to the dissolution process in which the α/β boundary moves outward. Hence, it includes the challenges associated with accurately tracking the motion of a phase boundary possessing a discontinuity in the nitrogen concentration. There are two simplifications however: 1) the conjugate nitriding process does not require a description of the complex transport conditions at the *S/L* interface; and 2) there is no motion of the *S/L* phase boundary. The details of the nitriding model development and its validation against experimentally derived data are presented in Chapter 4.

Chapter 5 presents the development of two numerical models describing the dissolution of spherical *Ti-N* inclusions in liquid titanium. Model 1 was developed based on the methodology of previously published dissolution models. Model 2 was developed using the model framework developed in Chapter 4. Model 2 was then used to examine the main factors influencing the dissolution kinetics of an inclusion.

3.2 **Objectives of the research program**

The objectives can be summarised as follows:

1. Develop a numerical modeling framework that describes the transport of nitrogen in CP titanium at elevated temperatures. The framework should be amenable to describing the nitriding of CP titanium at 1650°C and the dissolution of *Ti-N* inclusions in liquid titanium.

2. Validated the numerical modelling framework against a combination of analytical solutions, experimentally derived data and an alternative modeling approach previously described in the literature.

3. Use the dissolution model to investigate the dissolution kinetics of *Ti-N* inclusions in liquid titanium by conducting a sensitivity analysis to slip velocity, fluid temperature, nitrogen diffusion coefficients, and nitrogen solubility limits.

Chapter 4 Numerical Modeling of the Diffusional Transport of Nitrogen in Multi-Phase Solid Titanium and its Application to Determine Diffusion Coefficients

This chapter presents the development of a numerical model to describe phase boundary migration in the *Ti-N* system as a function of nitrogen transport. The methodology follows an approach previously published on diffusion-controlled phase change in which a Landau transformation is applied to the equations governing solute diffusion and phase boundary motion [24]. [1]

4.1   Model Formulation

Previous works [18][25] examining the dissolution of *Ti-N* inclusions and the conjugate process of nitriding of titanium, report the presence of multiple solid phases. Figure 4-1 shows images of phase boundaries in samples from an experiments involving *Ti-N* dissolution in liquid titanium [18] and nitriding of commercially pure titanium (CP-Ti) at an elevated temperature [25]. *Note:* CP-Ti *typically contains 0.18-0.40 wt. % oxygen, 0.20-0.50 wt. % iron, and trace amounts of carbon and nitrogen (<0.10 wt. %)* [1]. This chapter presents the development of an analytical model for a semi-infinite geometry first as a means of generating data suitable for verification of the numerical model. The numerical model was then applied to a cylindrical geometry and the results compared to data derived from an experiment in which a rod of CP-Ti was exposed to an atmosphere enriched in nitrogen at an elevated temperature.

---

[1] This Chapter is based on a paper accepted for publication in Journal of Materials Research and Technology, June 2021, apart from the introduction, which has been removed to avoid unnecessary repetition.

(a)   (b)
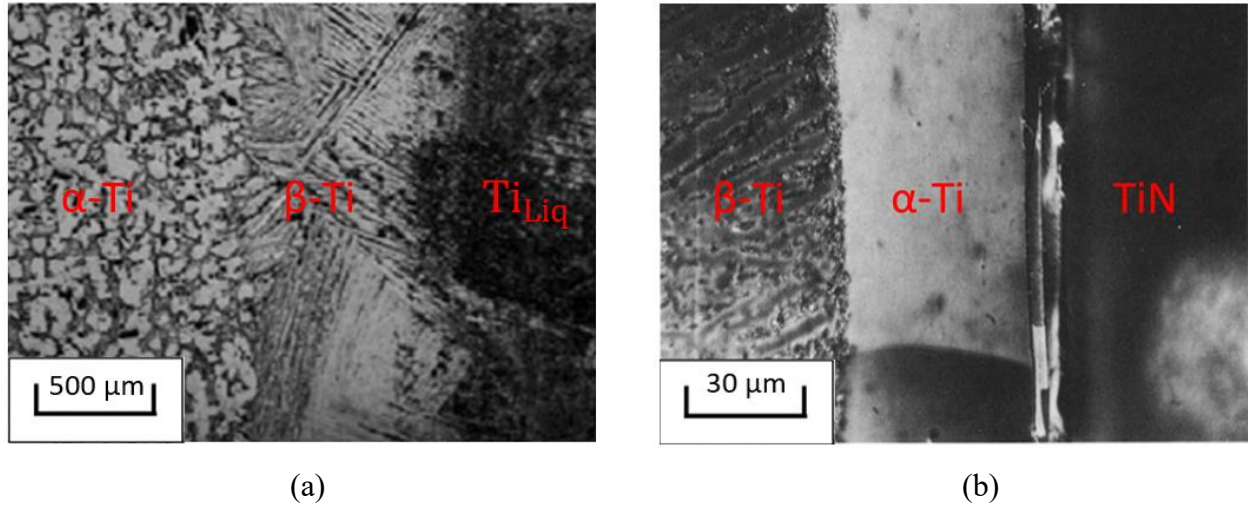
Figure 4-1. a) the microstructure of a *Ti-N* inclusion that has undergone dissolution. The labels (red text) represent the phases that are thought to be present when the dissolution process was occurring [18]. b) the microstructure of a CP-Ti sample that was exposed to a nitrogen rich atmosphere. The labels (red text) represent the phases that are thought to be present when the nitriding process was occurring [25].

4.1.1   Analysis Domains and Governing PDE's

Two geometries were used for the development of a 1-D numerical model: 1) a 5 mm wide plate, which, for short times, may be used to approximate a semi-infinite problem; and 2) a cylinder with a radius of 5 mm, used for analysis of the experiments involving a rod. Based on previously published results, the models must describe the transport of nitrogen in β-*Ti*, *α-Ti* and *TiN* phases; and the evolution of the phase boundary positions with time [19][25][26].

The models assume: 1) the system being modeled is isothermal; 2) the density is constant; 3) the diffusion coefficients are concentration independent within each phase; 4) the various phases grow as a front with the β-*Ti*/*α-Ti* and *α-Ti*/*TiN* phase fronts at chemical equilibrium – i.e. there is no nucleation of one phase within another; and 5) the system only contains titanium and nitrogen – i.e. the presence of oxygen, iron and trace elements is not considered.
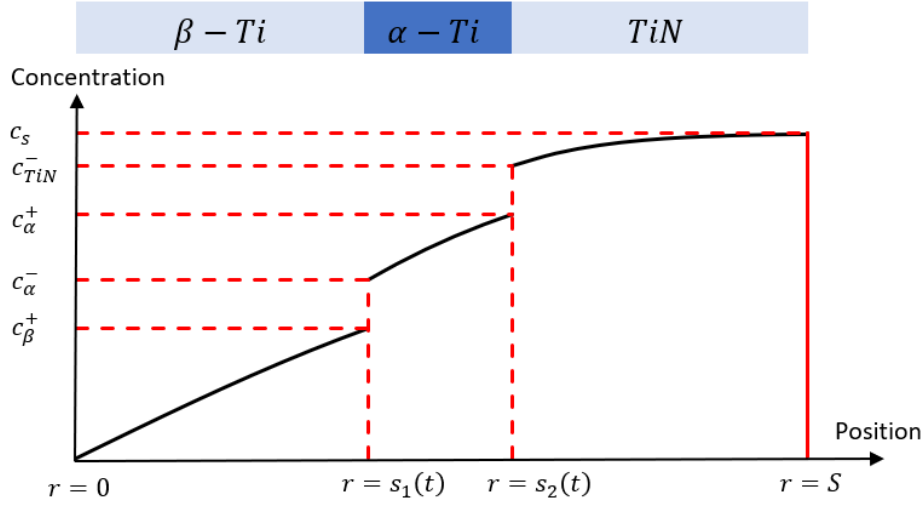
Figure 4-2. Schematic of a typical nitrogen concentration profile for nitrogen transport during the nitriding of CP-Ti.

Model development is focused on the nitriding problem as there is good data available for validation of the model. Referring to Figure 4-2, the introduction of nitrogen at the outer surface, $r = S$, results in nitrogen transport into the analysis domain and the motion of the phase boundaries inward with increasing time. Assuming that transport of nitrogen may be described by Fick's 2nd Law, the evolution in concentration within each phase is described by Eqs. 4.1-4.3 [20][27]:

$$r^{\lambda-1}\frac{\partial c}{\partial t} = \frac{\partial}{\partial r}\left(r^{\lambda-1}D_\beta\frac{\partial c}{\partial r}\right), \qquad 0 \leq r \leq s_1 \tag{4.1}$$

$$r^{\lambda-1}\frac{\partial c}{\partial t} = \frac{\partial}{\partial r}\left(r^{\lambda-1}D_\alpha\frac{\partial c}{\partial r}\right), \qquad s_1 \leq r \leq s_2 \tag{4.2}$$

$$r^{\lambda-1}\frac{\partial c}{\partial t} = \frac{\partial}{\partial r}\left(r^{\lambda-1}D_{TiN}\frac{\partial c}{\partial r}\right), \qquad s_2 \leq r \leq S \tag{4.3}$$

where s_1 [m] and s_2 [m] are the positions of the β-Ti/α-Ti and α-Ti/TiN phase boundaries, respectively, c [kg·m^{-3}] is the nitrogen concentration, t [s] is time, and D_i [m^2·s^{-1}] is the diffusion coefficient of nitrogen in phase i. Eqs. 4.1-4.3 sufficiently describe the nitrogen transport in this system and may be used to represent planar, cylindrical, and spherical geometries where the concentration is a function of a single positional parameter, r. The constant, λ, changes depending on the geometry - i.e. $\lambda = 1, 2, or 3$ for planar, cylindrical, or spherical cases, respectively.

The governing equations that describe phase boundary motion are determined from the mass conservation of nitrogen on either side of the phase boundary [20][24]. If the nitrogen mass fluxes

are not equal, conservation of mass enforces motion of the phase boundary. The motion of the phase boundaries is given by Eqs. 4.4 and 4.5.

$$D_\beta \frac{\partial c}{\partial r}\Big|_{r=s_1^-} - D_\alpha \frac{\partial c}{\partial r}\Big|_{r=s_1^+} = [c_\alpha^- - c_\beta^+]\frac{ds_1}{dt}, \qquad r = s_1 \tag{4.4}$$

$$D_\alpha \frac{\partial c}{\partial r}\Big|_{r=s_2^-} - D_{TiN} \frac{\partial c}{\partial r}\Big|_{r=s_2^+} = [c_{TiN}^- - c_\alpha^+]\frac{ds_2}{dt}, \qquad r = s_2 \tag{4.5}$$

where c_i^- [kg·m⁻³] is the lower nitrogen concentration limit in phase i and c_i^+ [kg·m⁻³] is the upper nitrogen concentration limit in phase i.

4.1.2 Analytical model

Previous authors have developed closed-form analytical solutions for the set of non-linear differential Eqs. 4.1-4.5 for semi-infinite and infinite geometries [28][29]. The following analytical solution is derived for a semi-infinite slab of CP-Ti held at 1650 °C. The initial and boundary conditions are as follows: the initial width of the α-Ti and TiN phases are zero and the initial concentration of nitrogen within the domain c_0 is set to 0 – i.e. $c(r,0) = c_0$. A Dirichlet boundary condition is applied in which the surface concentration is instantaneously increased and held at c_S – i.e. $c(S,t) = c_S$. This assumes that a layer of stoichiometric TiN is formed instantaneously at the surface of the analysis domain.

It is convenient to introduce rate constants, $b_{\beta\alpha}$ and $b_{\alpha TiN}$, to describe the phase boundary motion, such that $s_1 = b_{\beta\alpha}\sqrt{t}$ and $s_2 = b_{\alpha TiN}\sqrt{t}$. For the three-phase Ti-N system, five governing equations are needed to describe nitrogen transport. The nitrogen concentrations in each phase as a function of position and time are described by Eqs. 4.6-4.8 [28]:

$$c_\beta(r,t) = c_0 + (c_\beta^+ - c_0)\frac{\mathrm{erf}\left(\dfrac{r}{2\sqrt{D_\beta t}}\right) + 1}{\mathrm{erf}\left(\dfrac{b_{\beta\alpha}}{2\sqrt{D_\beta}}\right) + 1}, \qquad r \leq s_1 \tag{4.6}$$

$$c_\alpha(r,t) = c_\alpha^+ + (c_\alpha^- - c_\alpha^+)\frac{\mathrm{erf}\left(\dfrac{r}{2\sqrt{D_\alpha t}}\right) - \mathrm{erf}\left(\dfrac{b_{\alpha TiN}}{2\sqrt{D_\alpha}}\right)}{\mathrm{erf}\left(\dfrac{b_{\beta\alpha}}{2\sqrt{D_\alpha}}\right) - \mathrm{erf}\left(\dfrac{b_{\alpha TiN}}{2\sqrt{D_\alpha}}\right)}, \qquad s_1 \leq r \leq s_2 \tag{4.7}$$

$$c_{TiN}(r,t) = c_S + (c_{TiN}^- - c_S)\frac{\mathrm{erf}\left(\frac{r}{2\sqrt{D_{TiN}t}}\right) - \mathrm{erf}\left(\frac{S}{2\sqrt{D_{TiN}t}}\right)}{\mathrm{erf}\left(\frac{b_{\alpha TiN}}{2\sqrt{D_{TiN}}}\right) - \mathrm{erf}\left(\frac{S}{2\sqrt{D_{TiN}t}}\right)}, \quad s_2 \leq r \leq S \tag{4.8}$$

The solutions to the phase boundary motion equations are solved by first differentiating Eqs. 4.6-4.8 with respect to position and substituting the resulting expressions into Eqs. 4.4-4.5. The following two equations describe the motion of the phase boundaries:

$$\frac{\sqrt{\pi}(c_\alpha^- - c_\beta^+)b_{\beta\alpha}}{2} = \frac{\sqrt{D_\beta}(c_\beta^+ - c_0)e^{-\left(\frac{b_{\beta\alpha}^2}{4D_\beta}\right)}}{\mathrm{erf}\left(\frac{b_{\beta\alpha}}{2\sqrt{D_\beta}}\right) + 1} - \frac{\sqrt{D_\alpha}(c_\alpha^- - c_\alpha^+)e^{-\left(\frac{b_{\beta\alpha}^2}{4D_\alpha}\right)}}{\mathrm{erf}\left(\frac{b_{\beta\alpha}}{2\sqrt{D_\alpha}}\right) - \mathrm{erf}\left(\frac{b_{\alpha TiN}}{2\sqrt{D_\alpha}}\right)} \tag{4.9}$$

$$\frac{\sqrt{\pi}(c_{TiN}^- - c_\alpha^+)b_{\alpha TiN}}{2} = \frac{\sqrt{D_\alpha}(c_\alpha^- - c_\alpha^+)e^{-\left(\frac{b_{\alpha TiN}^2}{4D_\alpha}\right)}}{\mathrm{erf}\left(\frac{b_{\beta\alpha}}{2\sqrt{D_\alpha}}\right) - \mathrm{erf}\left(\frac{b_{\alpha TiN}}{2\sqrt{D_\alpha}}\right)} - \frac{\sqrt{D_{TiN}}(c_{TiN}^- - c_s)e^{-\left(\frac{b_{TiN\alpha}^2}{4D_{TiN}}\right)}}{\mathrm{erf}\left(\frac{b_{TiN\alpha}}{2\sqrt{D_{TiN}}}\right) - \mathrm{erf}\left(\frac{S}{2\sqrt{D_{TiN}t}}\right)} \tag{4.10}$$

The phase boundary rate constants, $b_{\beta\alpha}$ and $b_{\alpha TiN}$ are required to solve Eqs. 4.6–4.10. The method used to determine the rate constants is discussed in the Results and Discussion section.

4.1.3   Numerical model

Numerical Methodology - Due to discontinuities in the nitrogen concentration profile at the phase boundaries, numerical errors can arise during the tracking of boundary positions and subsequent adjustment of the nitrogen concentration profile [21]. Illingworth et al. [20] discuss three distinct approaches that offer the potential to solve diffusion-controlled phase change problems numerically. In the first method, space is discretized with a fixed mesh requiring the phase boundary to move in a stepwise manner such that the phase boundary will always coincide with a mesh node. Although methods for this approach have been developed for planar, cylindrical, and spherical systems, this approach is challenging for a system with multiple phase boundaries.

In an alternative approach, the governing equations are written in terms of the chemical activity of a solute instead of solute concentration [30]. The chemical activity of a solute varies continuously across a domain, providing a tractable solution for solute diffusion within a multi-phase system. Unfortunately, no experimental data could be found on the activity of nitrogen in titanium at 1650°C.

Finally, a method has been developed which introduces a coordinate system in which all phase boundaries were fixed. Landau first introduced this method before Murray and Landis applied the method to solve problems numerically [31][32]. An early application to a diffusion-controlled phase change occurred in 1968 when the method was utilized by Tanzilli and Heckel [33]. Heckel and Lanam later reported an application of the Landau transformation to a system with multiple moving phase boundaries [24]. In the current model, the Landau transformation is applied, based on the method developed by Lanam and Heckel, to describe nitrogen transport in titanium.
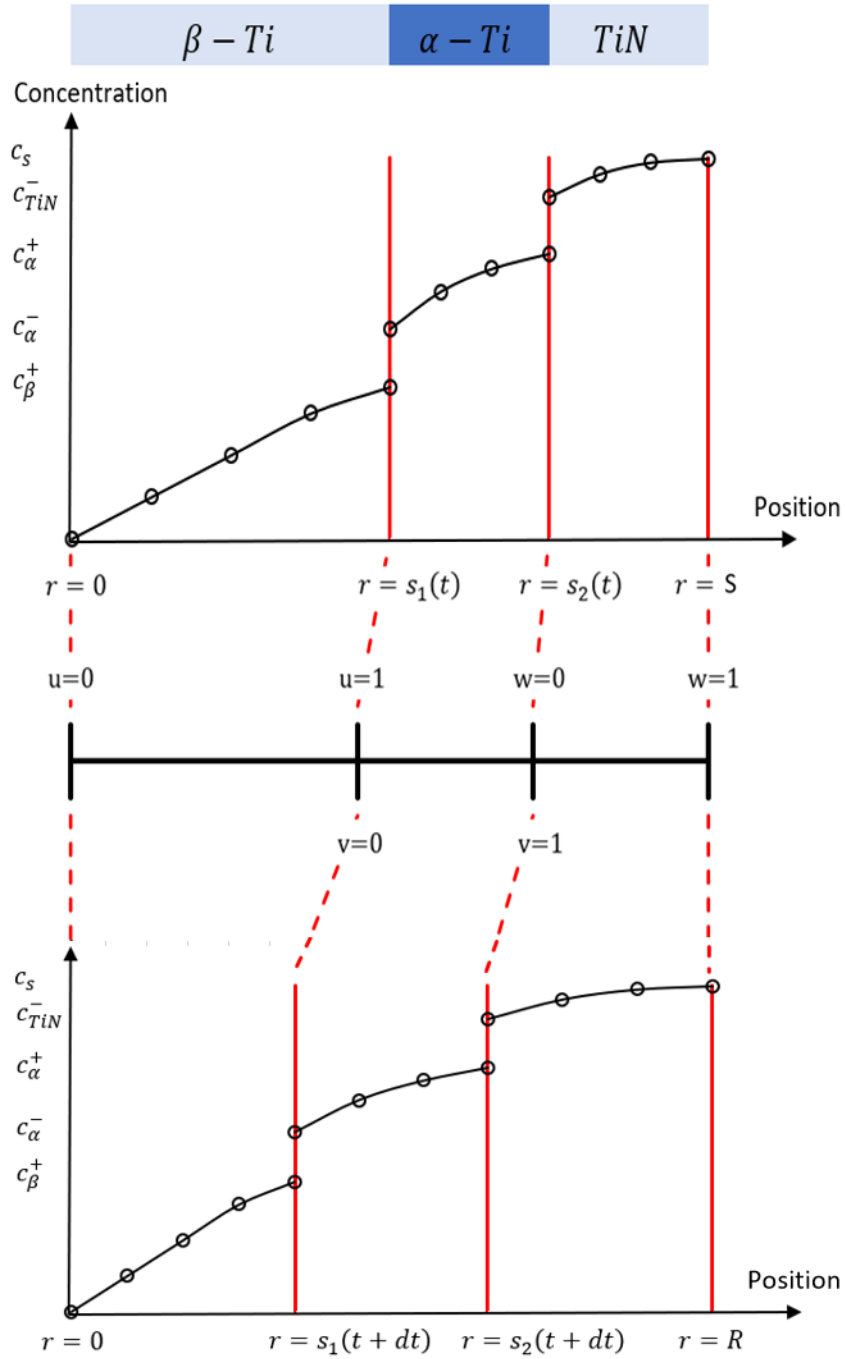
Figure 4-3. Schematic of nitrogen concentration profile as a function of position at times t and $t + dt$. The positional variables u, v and w for β-Ti, α-Ti and TiN phases will automatically adjust with the phase boundary motions such that the positional variables will always have a value between 0 and 1.

To simplify the numerical analysis, new positional variables, u, v, w are introduced for each phase boundary, with each having a range of values between 0 and 1. This is schematically

34

illustrated in Figure 4-3. For the β-Ti phase the positional variable r is replaced by u by setting $u = \frac{r}{s_1}$, such that $0 \leq u \leq 1$. Using the chain rule, Fick's Law may be rearranged in terms of the new positional variable to yield Eq. 4.11. For the α-Ti phase, the positional variable r, is replaced by v by setting $v = \frac{r - s_1}{s_2 - s_1}$ such that $0 \leq v \leq 1$, yielding Eq. 4.12. And, for the TiN phase, the positional variable r is replaced by w by setting $w = \frac{r - s_2}{S - s_2}$, such that $0 \leq w \leq 1$, resulting in Eq. 4.13.

$$(us_1)^{\lambda-1}\left(\frac{\partial c}{\partial t} - \left(\frac{u\frac{ds_1}{dt}}{s_1}\right)\frac{\partial c}{\partial u}\right) = \frac{\partial}{\partial u}\left(\frac{(us_1)^{\lambda-1}D_\beta}{s_1^2}\frac{\partial c}{\partial u}\right), \qquad 0 \leq u \leq 1 \qquad (4.11)$$

$$(s_1 + (s_2 - s_1)v)^{\lambda-1}\left(\frac{\partial c}{\partial t} + \left(\frac{(v-1)\frac{ds_1}{dt} - v\frac{ds_2}{dt}}{(s_2 - s_1)}\right)\frac{\partial c}{\partial v}\right)$$

$$= \frac{\partial}{\partial v}\left(\frac{(s_1 + (s_2 - s_1)v)^{\lambda-1}D_\alpha}{(s_2 - s_1)^2}\right)\frac{\partial c}{\partial v}, \qquad 0 \leq v \leq 1 \qquad (4.12)$$

$$(s_2 + (S - s_2)w)^{\lambda-1}\left(\frac{\partial c}{\partial t} - \left(\frac{(1-w)\frac{\partial s_2}{\partial t}}{(S - s_2)}\right)\frac{\partial c}{\partial w}\right)$$

$$= \frac{\partial}{\partial w}\left(\left(\frac{(s_2 + (S - s_2)w)^{\lambda-1}D_{TiN}}{(S - s)^2}\right)\frac{\partial c}{\partial w}\right), \qquad 0 \leq w \leq 1 \qquad (4.13)$$

Applying the chain rule, the equations that describe the phase boundary motions are rewritten in terms of the transformed positional variables u, v, and w - see Eqs. 4.14 and 4.15.

$$\left(\frac{D_\beta}{s_1}\right)\frac{\partial c}{\partial u}\Big|_{u=1} - \left(\frac{D_\alpha}{s_2 - s_1}\right)\frac{\partial c}{\partial v}\Big|_{v=0} = [c_\alpha^- - c_\beta^+]\frac{ds_1}{dt} \qquad (4.14)$$

$$\left(\frac{D_\alpha}{s_2 - s_1}\right)\frac{\partial c}{\partial v}\Big|_{v=1} - \left(\frac{D_{TiN}}{S - s_2}\right)\frac{\partial c}{\partial w}\Big|_{w=0} = [c_{TiN} - c_\alpha]\frac{ds_2}{dt} \qquad (4.15)$$

In order to implement the numerical model, Eqs. 4.10-4.15 are linearized and solved using a finite difference scheme. For Eqs. 4.16-4.18, an explicit finite difference scheme is used in which the compositional at the future timestep is expressed in terms of the values at the current time step.

The discretized forms of the equations are presented in Eqs. 16-18. *Note: the discretized versions of Eqs. 11-13 could not be written in a general form to describe the planar, cylindrical and spherical geometries. Eqs. 16-18 are only applicable to planar and cylindrical geometries, which are the focus of this work.*

$$\frac{c_l^{p+1} + c_l^p}{\Delta t} = \frac{D_\beta (c_{l+1}^p - 2c_l^p + c_{l-1}^p)}{(s_1^p)^2 (\Delta u)^2} + \left(\frac{s_1^{p+1} - s_1^p}{\Delta t}\right)\left(\frac{u}{s_1^p}\right)\left(\frac{c_{l+1}^p - c_{l-1}^p}{2\Delta u}\right)$$

$$+ \left(\left(\frac{D_\beta}{s_1^2 u}\right)\left(\frac{c_{l+1}^p - c_{l-1}^p}{2\Delta u}\right) + 1\right)^{\lambda - 1} - 1, \qquad 0 \le u \le 1 \tag{4.16}$$

$$\frac{c_m^{p+1} + c_m^p}{\Delta t} = \frac{D_\alpha (c_{m+1}^p - 2c_m^p + c_{m-1}^p)}{(s_2^p - s_1^p)^2 (\Delta v)^2}$$

$$+ \left(v\left(\frac{s_2^{p+1} - s_2^p}{\Delta t}\right)\right.$$

$$- (v - 1)\left(\frac{s_1^{p+1} - s_1^p}{\Delta t}\right)\right)\left(\frac{1}{s_2^p - s_1^p}\right)\left(\frac{c_{m+1}^p - c_{m-1}^p}{2\Delta v}\right) \tag{4.17}$$

$$+ \left(\left(\frac{D_\alpha}{(s_1^p + (s_2^p - s_1^p)v)(s_2^p - s_1^p)}\right)\left(\frac{c_{m+1}^p - c_{m-1}^p}{2\Delta v}\right) + 1\right)^{\lambda - 1}$$

$$- 1, \qquad 0 \le v \le 1$$

$$\frac{c_n^{p+1} + c_n^p}{\Delta t} = \frac{D_{TiN} (c_{n+1}^p - 2c_n^p + c_{n-1}^p)}{(S - s_2^p)^2 (\Delta w)^2}$$

$$+ \left(\frac{s_2^{p+1} - s_2^p}{\Delta t}\right)\left(\frac{1 - w}{S - s_2^p}\right)\left(\frac{c_{n+1}^p - c_{n-1}^p}{2\Delta w}\right)$$

$$+ \left(\left(\frac{D_{TiN}}{(s_2^p + (S - s_2^p)w)(S - s_2^p)}\right)\left(\frac{c_{n+1}^p - c_{n-1}^p}{2\Delta w}\right) + 1\right)^{\lambda - 1} - 1, \tag{4.18}$$

$$0 \le w \le 1$$

where the subscripts *l, m and n,* on the concentration terms, denote the node numbers in *β-Ti*, *α-Ti* and *TiN* phases, respectively. The superscript p denotes the timestep. The positional variables at the future timestep are estimated based on Eqs. 4.19-4.20, which describe the mass balance across the interfaces.

$$\left(\frac{D_\beta}{s_1}\right)\frac{(-c^p_{L-2} + 4c^p_{L-1} - 3c^+_\beta)}{2\Delta u} - \left(\frac{D_\alpha}{s_2 - s_1}\right)\frac{(c^p_{m=2} - 4c^p_{m=1} + 3c^-_\alpha)}{2\Delta v}$$

$$= (c^-_\alpha - c^+_\beta)\frac{(s^{p+1}_1 - s^p_1)}{\Delta t} \tag{4.19}$$

$$\left(\frac{D_\alpha}{s_2 - s_1}\right)\frac{(-c^p_{M-2} + 4c^p_{M-1} - 3c^+_\beta)}{2\Delta v} - \left(\frac{D_{TiN}}{S - s_2}\right)\frac{(+c^p_{n=2} - 4c^p_{n=1} + 3c^-_\alpha)}{2\Delta w}$$

$$= (c_{TiN} - c_\alpha)\frac{(s^{p+1}_2 - s^p_2)}{\Delta t} \tag{4.20}$$

where subscripts L and M denote the node number at the phase interfaces in β-*Ti* and α-*Ti*.

At the beginning of each time step, Eqs. 4.19 – 4.20 computes the rate of change of the positions of the interfaces. The computed rates are utilised in Eqs. 4.16-4.18 to determine the nitrogen concentration at each nodal point in β-*Ti*, α-*Ti* and *TiN* phases. Finally, the interface positions (s_1 and s_2) are updated according to the rate of change of the interfaces. The solution algorithm then moves to the next time step.

This approach offers the opportunity to further enhance the model for both non-isothermal problems and/or problems in which varying density needs to be considered, which is beyond the scope of this work.

Phase Interface Concentrations - Previous studies modeling nitrogen diffusion in titanium have used the binary phase diagram to obtain the nitrogen concentrations at the various phase boundaries [18][14]. The concentration values were extracted from the phase diagram by finding the interception points of a horizontal line, at the temperature of interest (1650°C), with the lines denoting the single-phase concentration limit. A review of some of the published data indicates considerable variation [34]. The reader is referred to reference [26] for a description of the method used.

Table 4-1 summarizes some of the equilibrium concentration data. The values reported by Xu et al. [26] are shown in the bottom row ofThe reader is referred to reference [26] for a description of the method used.

Table 4-1 and are used as the phase boundary concentrations for this model. These concentration values were chosen because the model results are compared with nitrogen concentration profiles and phase location data extracted from the same study. The reader is referred to reference [26] for a description of the method used.

Table 4-1. Summary of the boundary concentration values at 1650 °C for the titanium-nitrogen system [26].

c_β^+ (wt. %)	c_α^- (wt. %)	c_α^+ (wt. %)	c_{TiN}^+ (wt. %)	Ref.
1.43	2.84	6.80	9.22	[35]
1.40	4.55	4.79	7.9	[36]
2.62	5.24	6.48	6.67	[26]

Boundary and Initial Conditions – For analysis of the semi-infinite planar problem, $\lambda = 1$, the boundary conditions are $\left(\frac{\partial c}{\partial r}\right)|_{r=0} = 0$ and $c(r,t) = c_s$ at $r = S$. The initial condition is $c(r,0) = c_0$, where $c_0 = 0$. The boundary condition at $r = 0$ limits the time for which the numerical solution can be compared to the analytical solution to times $t < t_{max}$ where t_{max} is defined as the time at which $c(0,t) > c_0$. For the analysis of the rod, $\lambda = 2$, the same boundary and initial conditions are applied.

CP-Ti held at 1650 °C with no nitrogen present - i.e. $c(r, 0) = 0$ will contain only *β-Ti* phase. However, in the current version of the numerical model, the formulation does not account for the nucleation of the *β-Ti, α-Ti* and *TiN* phases and therefore the domain must be initialized with a small amount of each phase present.

For the plate domain, the approach is to initialize the nitrogen concentration profile and phase boundary positions from the semi-infinite analytical solution in which the exposure to a nitrogen rich atmosphere is limited to a short time of 1 s. This ensures a reasonable "starting condition" for the numerical analysis.

For the rod domain, there is no equivalent analytical solution and so the same approach as adopted for the plate has been used. For the short analysis time (1 s), it is assumed that the semi-infinite planar solution would not introduce significant error.

Material Properties - The diffusion coefficient for nitrogen in *β-Ti, α-Ti* and *TiN* has been studied by a limited number of authors [19] [37]. The diffusion coefficients used by Bellot et. al. [14] are implemented in this numerical model for the *β-Ti* and *α-Ti* phases, while the diffusion coefficient used by L'Enfant et al. [19] is implemented in this numerical model for the *TiN* phase.

$$D_\beta = 4.6 \times 10^{-5} \exp\left(-\frac{185 \times 10^3}{RT}\right) \tag{4.16}$$

$$D_\alpha = 3.1 \times 10^{-7} \exp\left(-\frac{168 \times 10^3}{RT}\right) \tag{4.17}$$

$$D_{TiN} = 2.7 \times 10^{-7} \exp\left(-\frac{180 \times 10^3}{RT}\right) \tag{4.18}$$

where R [J·mol^{-1}·k^{-1}] is the ideal gas constant.

Analysis Domain – As previously described, two geometries were used for the development of a 1-D numerical model: 1) a 5 mm wide plate; and 2) a cylinder with a radius of 5 mm. Following the approach for initialization, both models discretized each phase using a fixed number of equally spaced nodal points. A sensitivity analysis was conducted on node spacing by varying the node count in each of the three phase regimes. The results of this showed 100, 5 and 5 nodes for the β-Ti, *α-Ti* and *TiN* phases, respectively, to be sufficient – i.e., further refinement showed no substantial change in the predictions. For the model to function correctly nodal points must be present at each phase boundary – i.e., nodal points at *u, v, w* = 0 and 1.

4.2   **Results and Discussion**

4.2.1   **Numerical Model - Planar Domain**

Stability, robustness, and accuracy of the numerical model of a finite plate was assessed by comparing the phase boundary locations and the nitrogen concentration profiles predicted by the numerical model with analytical solutions for a semi-infinite plate derived from Eqs. 4.6-4.10. To obtain quantitative results from the analytical solution, approximate values for the rate constants, b$_{\beta\alpha}$ and b$_{\alpha TiN}$, were calculated using a trial-and-error approach. A solver was developed, in the programming language C, in which the value of each rate constant was varied incrementally over a given range. For each rate constant value, Eqs. 4.9-4.10 were evaluated and the percentage

differences between the left-hand side and right-hand side of Eqs. 4.9-4.10 were calculated. This process was continued until the sum of the percentage differences for the two equations was reduced to below the chosen margin of error (0.1 %).

The analytical solution predicts the phase boundaries will move in a parabolic relationship with time. Figure 4-4 shows this behaviour is also predicted by the numerical model up to a time, $t <$ ~9500s . The numerical and analytical results begin to diverge at t_{max}=~9500s, where t_{max} is the time at which the difference between the analytical and numerical results exceeds 1 %. For $t >$ ~9500s, the boundary condition applied at $r = 0$ in the numerical solution ceases to mimic the semi-infinite condition. The divergence between the analytical and numerical models arises from the numerical model's finite representation. As the phase boundaries advance along the flat plate, the discrepancy between the semi-infinite (analytical) and finite (numerical) boundary conditions results in different concentration gradients and, therefore, the discrepancy in the phase boundary locations at longer simulated times.
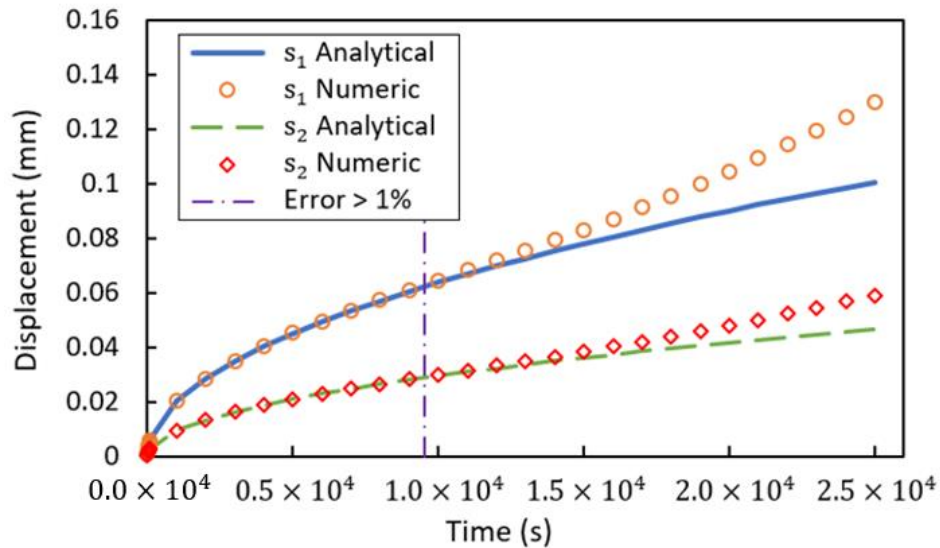
Figure 4-4. The displacements of the phase boundaries, s₁ and s₂, are presented as a function of time for the numerical result for a 5 mm wide plate and the analytical result for a semi-infinite plate.

Figure 4-5 presents a comparison of the nitrogen concentration profiles from the numerical result and analytical solution after 1000 s of nitriding and shows the profiles to be in excellent agreement. In combination, Figure 4-4 and Figure 4-5 indicate the numerical model, developed using a Landau transformation, can approximate solute transport in a diffusion-controlled system

in which there are three phases present. Further, the difference in solubilities and diffusion coefficients in the three phases is consistent with that observed in the *Ti-N* system indicating the approach is suitable for analysis in the *Ti-N* system.
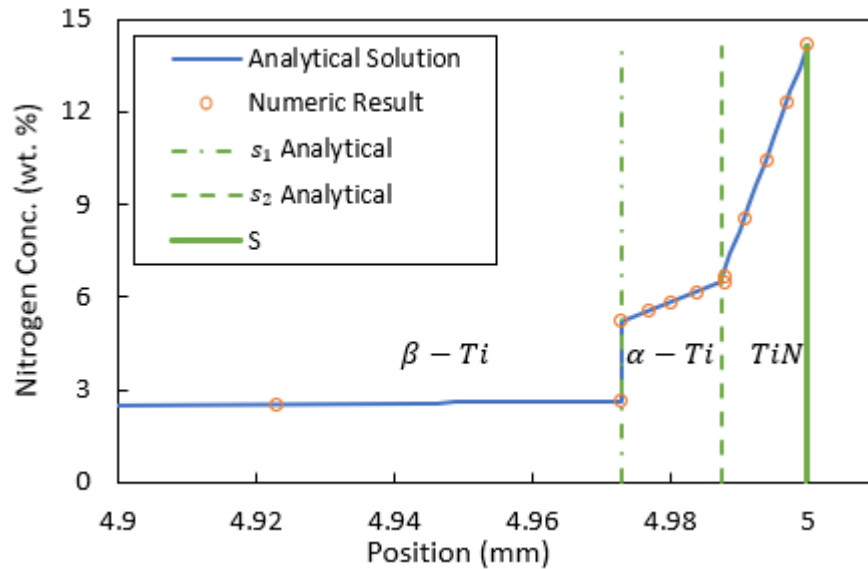
Figure 4-5. The nitrogen concentration profiles are presented at $t = 1000$ s for the numerical results for a 5 mm wide plate and analytical results for a semi-infinite plate.

4.2.2   Numerical Model – Cylindrical Domain

The experimental conditions reported in a study by Xu et al. [26] were incorporated into the numerical model, and a comparison between the model and experimental results is presented to validate the numerical model for a cylindrical domain. Xu et al. exposed CP-Ti rods to a nitrogen-rich atmosphere at 1650 °C in an induction furnace. The experimentally prepared rods were nitrided for 45,000 s, 88,200 s, and 174,600 s. The phases present, the phase boundaries, and the nitrogen concentration profiles of each rod were determined using microhardness analysis and x-ray diffraction techniques.

Figure 4-6 plots the predicted and measured displacements of the β-*Ti*/α-*Ti* phase boundary (s_1) and α-*Ti* /*TiN* phase boundary (s_2) as a function of time. For the β-*Ti*/α-*Ti* phase boundary, the error in the predicted displacements are 16.9 %, 13.0 % and 6.1 % at 45,000 s, 88,200 s, and 174,600 s, respectively, with the error trending to decrease with increasing time. For the α-*Ti*/*TiN* phase boundary, the numerical model overpredicts the phase boundary displacement by 15.5 %,

51.1 % and 80.3 % at 45,000 s, 88,200 s, and 174,600 s, respectively, with the error trending to increase with increasing time. Figure 4-7 demonstrates that discrepancies are also present between the nitrogen concentration profiles predicted by the numerical model and the experimentally measured profiles in the α-Ti and the TiN phases.
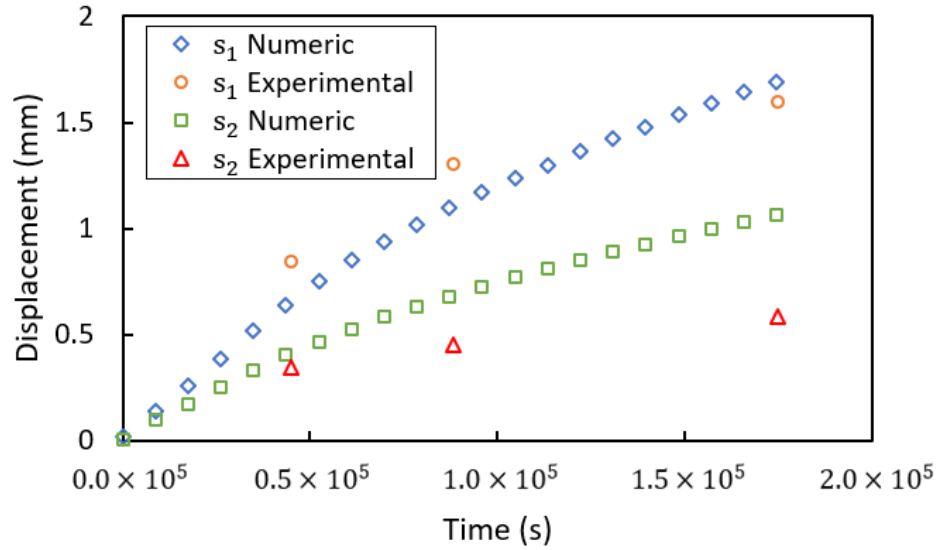
Figure 4-6. The phase boundary displacements are presented as a function of time for the numerical and experimental results [26] for a rod of radius 5 mm. In the numerical model, $D_\alpha = 8.47 \times 10^{-12}$ m²·s⁻¹ and $D_{TiN} = 3.48 \times 10^{-12}$ m²·s⁻¹.
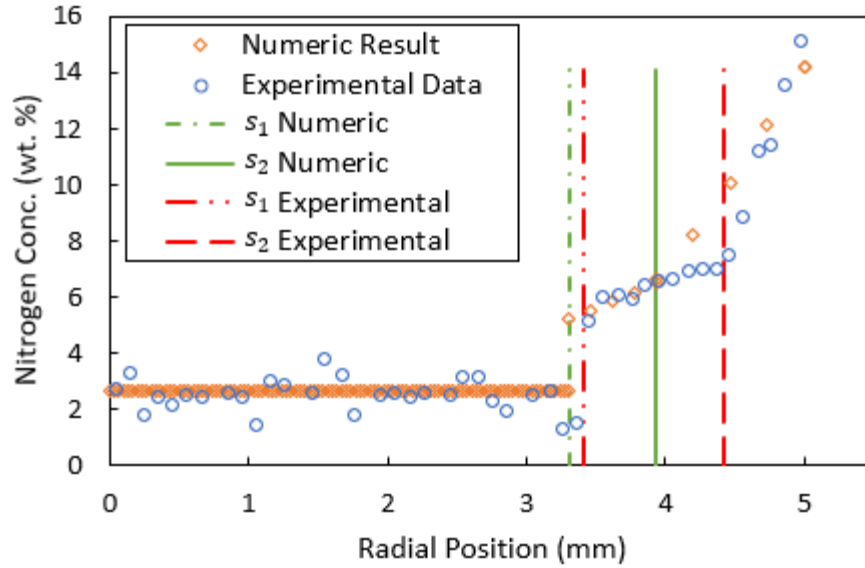
Figure 4-7. The nitrogen concentration profiles are presented for the numerical and experimental results [26] for a rod of radius 5 mm at 174,600 s. In the numerical model, $D_\alpha = 8.47 \times 10^{-12}$ m$^2\cdot$s^{-1} and $D_{TiN} = 3.48 \times 10^{-12}$ m$^2\cdot$s^{-1}.

The quantitative disagreement between the predicted and measured phase boundary displacements and concentration profiles may be a result of one or a combination of the following:

1. The model assumes that the diffusion coefficients are constant within each phase. Diffusion coefficients can vary significantly as a function of solute concentration within solid phases. However, non-linear solute concentration gradients would be observed in the solute concentration profile, which is not the case, indicating that it is valid to assume the diffusion coefficients are constant within each phase.

2. The model framework is built assuming that only β-*Ti*, *α-Ti* and *TiN* phases are present at the time of nitriding. This assumption is based on microstructural analysis conducted at room temperature. This necessarily requires some interpretation of the results utilizing the binary *Ti-N* phase diagram, to determine what was present at the nitriding temperature, 1650 °C. It is possible that other phases are present at the time of nitriding. 38 years after the publication of the first *Ti-N* phase diagram, through a nitriding experiment, Lengauer [10] demonstrated that ξ-*Ti₄N₃* and η-*Ti₃N₂-ₓ* phases exist in a narrow range of nitrogen concentration and temperatures. However, only β-*Ti*, *α-Ti* and *TiN* have been shown to exist at 1650 °C in the *Ti-N* system. Additionally, as shown by Xu et al. [26], interpretation of the microstructure for a *Ti-N* rod at 1650 °C suggests

43

only the three phases are present at the time of nitriding. Therefore, the three-phase assumption is likely to be representative of the *Ti-N* system at 1650 °C.

3. Review of current literature suggests there is a lack of consensus on the nitrogen concentration limits and the diffusion coefficients for nitrogen in β-*Ti*, α-*Ti* and *TiN* phases. The nitrogen concentration limits input to the numerical model were based on explicit experimental analysis and, therefore, are not considered to contribute significantly to the observed discrepancies. In contrast, the diffusion coefficients were selected based on published data. A review of published data indicates a lack of consensus on the diffusion coefficients for nitrogen in β-*Ti*, α-*Ti* and *TiN* phases. Using inaccurate diffusion coefficients in the numerical model for α-*Ti* and *TiN* phases would explain why the model accurately describes the motion of the β-*Ti*/α-*Ti* phase boundary but significantly overpredicts the motion of the α-*Ti*/*TiN* phase boundary.

Given there is significant variance in the published diffusion coefficients for nitrogen in CP-Ti at elevated temperatures, a sensitivity analysis of phase boundary displacements to the diffusion coefficients used in the model was conducted. The percentage change in the displacement of the phase boundaries after 174,600 s simulation time relative to a base-case numerical model was used as a quantitative measure of the numerical model's sensitivity to the diffusion coefficients. Eq. 4.19 was used to calculate the percentage displacement change. The base case numerical model used the diffusion coefficients presented in the section 4.1.3. The procedure involved varying each of the β-*Ti*, α-*Ti* and *TiN* phase diffusion coefficients by 25% and 200% from their base-case values in sequence, while the diffusion coefficients in the other two phases were held constant at the base-case values.

$$s_i \; Displacement \; Error \; (\%) = \frac{(s_{i,BaseCase} - s_{i,})}{(S - s_{i,Basecase})} \times 100 \tag{4.19}$$

where $s_{i,BaseCase}$ is the position of phase boundary s_i in the base case model as described in section 4.1.3.

Figure 4-8 illustrates the sensitivity of the displacement of the s_1 and s_2 boundaries to systematic perturbation of the three diffusion coefficients. The α-*Ti*/*TiN* phase boundary shows sensitivity to changes in D_{TiN}, doubling D_{TiN} changes the α-*Ti*/*TiN* phase boundary displacement by 54.0 %. Additionally, the β-*Ti*/α-*Ti* phase boundary is sensitive to changes in D_α and D_{TiN}, doubling D_α

44

and D_{TiN} changes the β-*Ti*/α-*Ti* phase boundary displacement by 23.0 % and 26.0 %, respectively. However, changes in $D_β$ had little effect on the displacement of either phase boundary.
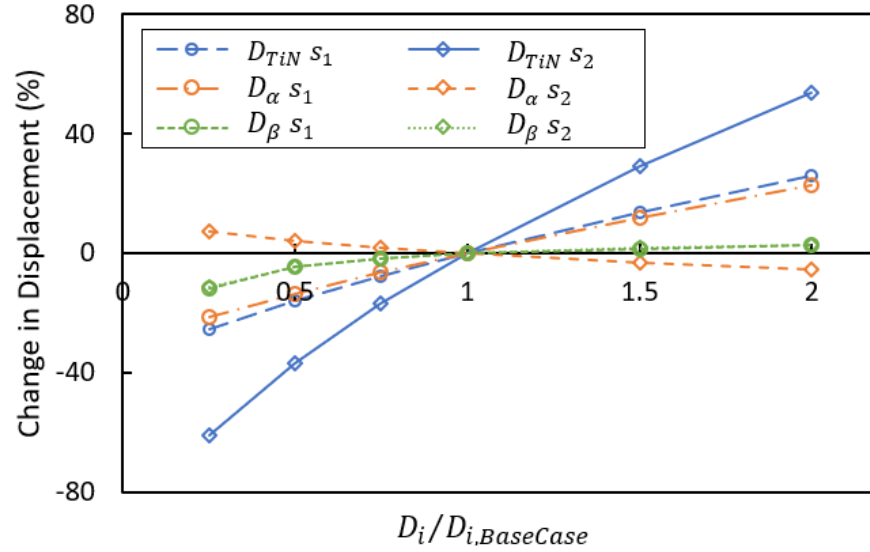
Figure 4-8. The numerical sensitivity of phase boundary displacement, predicted by the numerical model, is assessed as a function of the diffusion coefficient used for β-*Ti*, α-*Ti*, and *TiN* phases after 174,600 *s* run time in a rod of radius 5 mm.

The data presented in Xu's study [26] and in Figure 4-8 were analyzed and used to propose diffusion coefficients for nitrogen in α-*Ti* and *TiN* phases at 1650 °C of $1.60 \times 10^{-11} \ m^2 s^{-1}$ and $1.70 \times 10^{-12} \ m^2 s^{-1}$, respectively. The diffusion coefficients proposed are within the range reported in the published literature [25][19][38].

The numerical model was run using the proposed diffusion coefficients. Figure 4-9 shows that the phase boundary displacements predicted by the numerical model are now in good quantitative agreement with the experimentally derived data. The displacement errors are 12.4 % and 4.0 % for the β-*Ti*/α-*Ti* and α-*Ti*/*TiN* phase boundaries, respectively, after 174,600 s of nitrogen exposure. Figure 4-10 shows that the nitrogen concentration profiles predicted by the numerical model and the measured values are also now in good agreement.

45
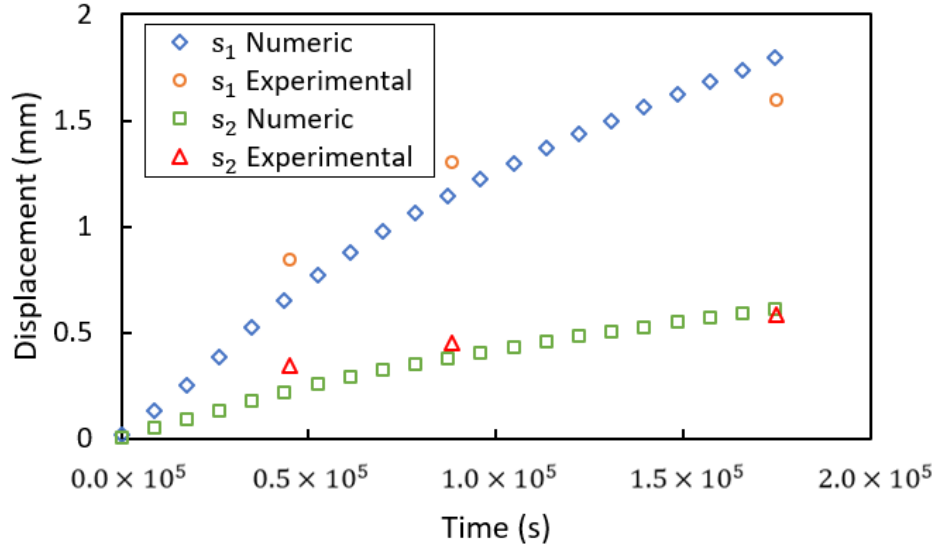
Figure 4-9. The phase boundary displacements, s_1 and s_2, as a function of time for the numerical and experimental results [26] for rod of radius 5 mm. In the numerical model, $D_\alpha = 1.60 \times 10^{-11}$ m²·s⁻¹ and $D_{TiN} = 1.7 \times 10^{-12}$ m²·s⁻¹.
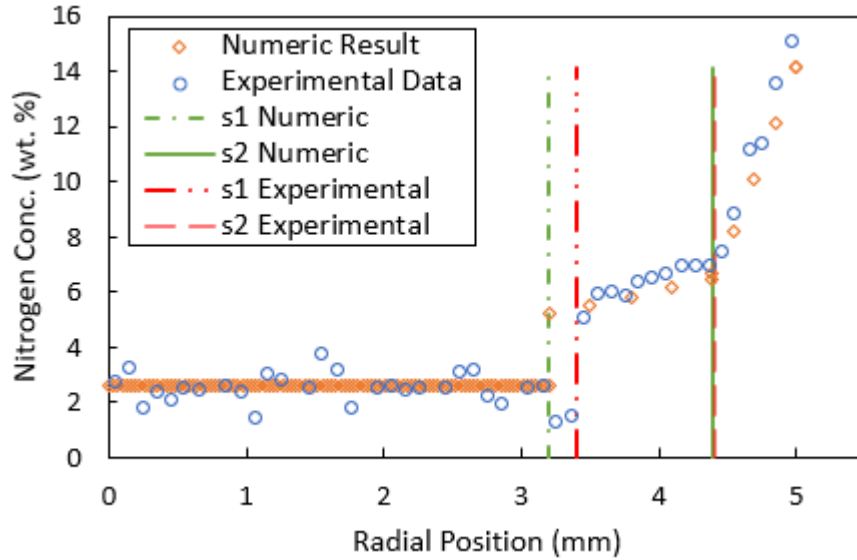
Figure 4-10. The nitrogen concentration profiles for the numerical and experimental results [26] for a rod of radius 5 mm at 174,600 s. In the numerical model, $D_\alpha = 1.60 \times 10^{-11}$ m²·s⁻¹ and $D_{TiN} = 1.7 \times 10^{-12}$ m²·s⁻¹.

A summary of reported diffusion coefficients at 1650 °C, including the values obtained from this work, is presented in Table 4-2. A comparison to data presented over a broader range of temperature is shown in Figure 4-11. In all the studies, a CP titanium specimen was exposed to a

nitrogen-rich atmosphere under isothermal conditions. The samples were held at temperature to allow nitriding to occur via the inward diffusion of nitrogen into the solid titanium matrix. Once allowed to cool to room temperature, microstructures of α'-Ti, α-Ti, ε-Ti$_2$N and δ-TiN$_X$ phases were reported [25][19][39]. An example of the phases identified was previously shown in Figure 4-1 (b). Although there is good agreement between the microstructures observed and a consensus on the overall mechanisms occurring during the nitriding process, it appears that there are significant disparities in the values obtained.

Generally, the diffusion coefficients were calculated by assuming that the growth kinetics of each phase follows a parabolic growth law, such that $s(t) = K^{0.5}t^{0.5}$, where K follows the Arrhenius law. Once the activation energy, Q, is estimated, D_0 in the expression for estimation of the diffusivity dependence on temperature (which is also typically Arrhenius) is fitted using analytical models for nitrogen transport. The models used are thought to be the same as the analytical model described in section 4.1.2. However, due to the limited information presented, this could not be confirmed. The current approach offers a robust method of estimating the diffusion coefficients in all the phases present providing the necessary experimental data is available.

Table 4-2. Summary of the diffusion coefficients for nitrogen in the titanium solid phases at 1650°C tabulated by author/reference.

Publication Author	D_α (m$^2\cdot$s^{-1})	D_{TiN} (m$^2\cdot$s^{-1})	Temperature Extrapolated	Author of Phase Diagram used
L'Enfant et al. [19]	8.29x10^{-12}	3.48 x10^{-12}	Yes	Lengauer [35]
Redkin et al. [39]	1.51 x10^{-11}	4.54 x10^{-13}	No	Palty et al. [40]
Bellot et al. [14]	8.47 x10^{-12}		No	Unknown
Eremeev et al. [38]	6.85 x10^{-12}	1.22 x10^{-13}	No	Palty et al. [40]
Bars et al. [25]	3.59 x10^{-12}		Yes	Palty et al. [40]
Bars et al. [25]	1.45 x10^{-11}		Yes	Toth [41]
This work	1.60 x10^{-11}	1.70 x10^{-12}	No	None
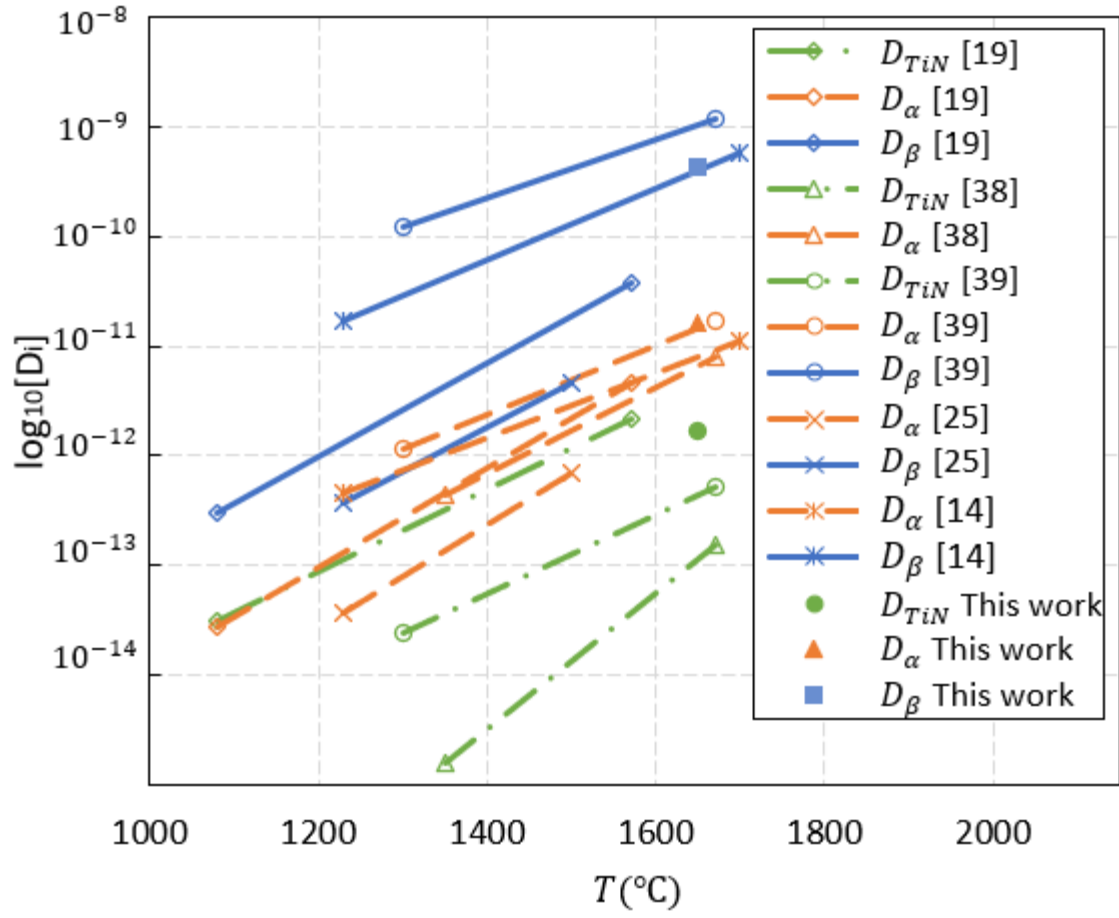
Figure 4-11. Diffusion coefficients as a function of temperature in β-*Ti*, α-*Ti* and *TiN* phases.

Chapter 5 Dissolution of *Ti-N* inclusions in liquid titanium

[2] As previously described, the dissolution of solid *Ti-N* inclusions in liquid titanium is an example of a Stefan problem as the diffusive transport of nitrogen, within the solid and from the boundary with the liquid, gives rise to two moving boundaries across which there is a discontinuity in nitrogen concentration: 1) a solid-solid boundary; and 2) a solid-liquid boundary. In numerical models, a moving phase boundary that results in a discontinuity in the solution variable must be tracked accurately within a domain that is discretized. For Stefan problems involving diffusive chemical species mass transport, Illingworth et al. [20] highlights that errors may arise when coupling Fick's second law, which describes mass diffusion within a given phase, with the mass balance equations used describe the phase boundary motion.

Caldwell et al. [21] notes that two conditions are required to accurately solve Stefan problems numerically, the solution of Fick's second law in all the phases present in the domain and the accurate tracking of the phase boundary position with time. Phase boundary motion is driven by differences in species mass in to and out of either side of the phase boundary. Mass conservation is imposed through motion of the boundary. In the numerical model, this motion occurs in discrete increments in space – i.e., the motion is dependent on the size of the timestep. Whereas in reality, the motion is smooth and spatially continuous.

Referring to Figure 5-1, which is used to illustrate the problem that arises numerically for the example problem of nitrogen removal from solid titanium, a mass imbalance across the interface will result in the incremental movement of the interface from its location at *t* to its location at *t+dt*. In Figure 5-1, the mass in the green region represents the incremental amount of mass (lost in the case shown) needed to "close" the imbalance. When the location of the interface is updated, and the composition of the node at the new position of the interface is set to the interface composition, there is the potential for an additional loss in mass associated with the pink region that is not accounted for. This additional loss has the potential to accumulate over time leading to an erroneous estimate of the dissolution rate of *Ti-N* particles. Studies by Caldwell et al. [21] and Illingworth et al. [20] discuss potential methods to accurately address this problem numerically.

---

[2] This chapter will be submitted shortly as a second manuscript and hence is presented in a format appropriate for publication.
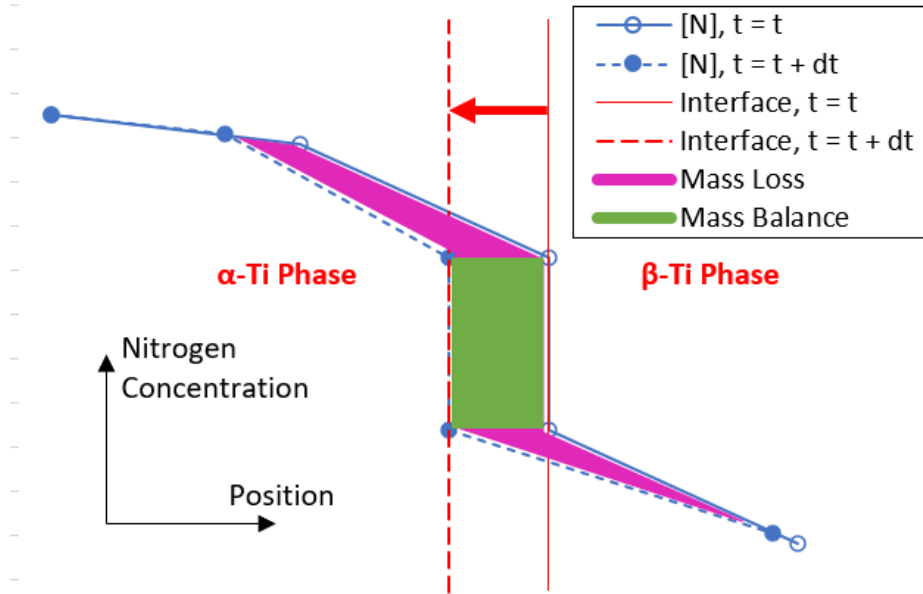
Figure 5-1. Schematic illustration of the *α-Ti*/β-*Ti* interface motion during *Ti-N* dissolution. The schematic shows the mass that is accounted for in standard mass balance equations (green region) and the mass that is not accounted for in standard mass balance equations (pink region).

This Chapter presents the development of two numerical models, which describe the dissolution of spherical *Ti-N* inclusions in a liquid titanium. Both models have been formulated to describe the motion of the *α-Ti*/β-*Ti* and β-*Ti*/Ti$_{Liq}$ phase boundaries using mass balance equations, and the transport of nitrogen within *α-Ti* and β-*Ti* solid phases using Fick's second law. The first model (Model 1) follows the development process used in a previously published model by Ghazal et al. [18]. Ghazal's approach does not appear to use any of the methods outlined by either Illingworth et al. or Caldwell et al to ensure accurate tracking of the phase interfaces. The second model (Model 2) follows the development process outlined in Chapter 4, where a Landau transformation is applied to the governing equations to accurately track the interface position and determine the nitrogen concentrations in *α-Ti* and β-*Ti* solid phases. In Chapter 4, modelling nitrogen transport via this approach was shown to be accurate by comparing the model outputs against analytical and experimental data.

The two models are first described and the results of the two compared to assess what if any difference is realized with the alternative approach. The second Landau-based model, Model 2, is then used to investigate the sensitivity of dissolution time to:1) material properties - e.g., the nitrogen diffusivities and phase composition limits; and 2) the process parameters – e.g., liquid metal temperature and particle slip velocity.

5.1 Model formulation

5.1.1 Analysis domains and governing PDE's

Both models are formulated using spherical coordinates and the distribution of nitrogen is assumed to be a function of the radius only. Each model describes the diffusional transport of nitrogen in α-Ti and β-Ti phases, the transport of nitrogen at the β-Ti/Ti$_{Liq}$ phase boundary, and the evolution of the phase boundary positions with time. The models assume: 1) the system being modeled is isothermal; 2) the density is constant; 3) the diffusion coefficients are concentration independent within each phase; and 4) the various phases grow as a front with the α-Ti /β-Ti and β-Ti/Ti$_{Liq}$ phase fronts at chemical equilibrium – i.e., there is no nucleation of one phase within another.
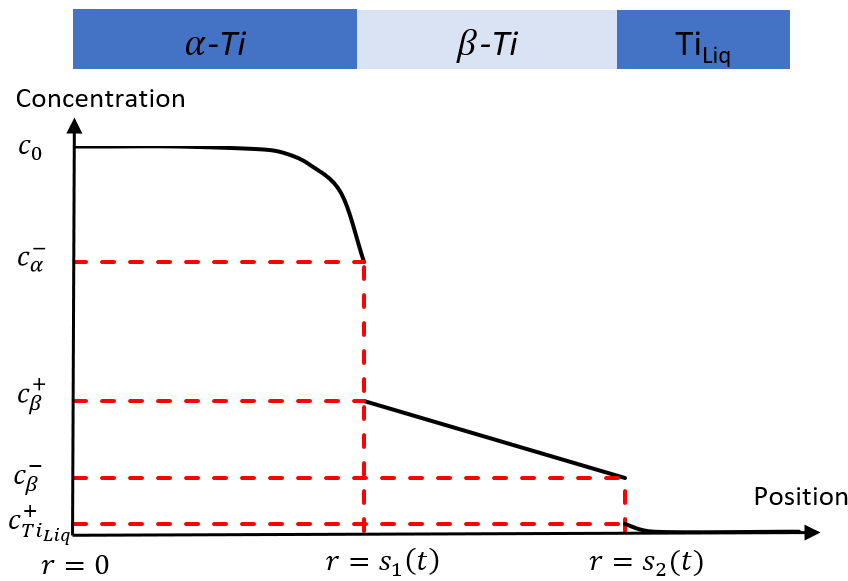
Figure 5-2. Schematic illustration of a typical concentration that occurs during dissolution.

Referring to Figure 5-2, the removal of nitrogen at the outer surface, $r = s_2$, causes the nitrogen concentration profiles to evolve and the phase boundaries to move with time. The models assume that the nitrogen transport in α-Ti and β-Ti phases are diffusion controlled and may be described by Fick's 2nd Law, the evolution in concentration within the phases is described by equations 5.1-5.2.

$$r^2 \frac{\partial c}{\partial t} = \frac{\partial}{\partial r}\left(r^2 D_\alpha \frac{\partial c}{\partial r}\right), \qquad 0 \leq r \leq s_1(t) \qquad (5.1)$$

51

$$r^2 \frac{\partial c}{\partial t} = \frac{\partial}{\partial r}\left(r^2 D_\beta \frac{\partial c}{\partial r}\right), \qquad s_1(t) \leq r \leq s_2(t) \tag{5.2}$$

where $s_1(t)$ [m] and $s_2(t)$ [m] are the positions of the α-Ti/β-Ti and β-Ti/Ti$_{Liq}$ phase boundaries, respectively, c [kg·m^{-3}] is the nitrogen concentration, t [s] is time, and D_i [m^2·s^{-1}] is the diffusion coefficient of nitrogen in phase i.

The governing equations that describe phase boundary motion are determined from the mass conservation of nitrogen on either side of the phase boundary. If the nitrogen mass fluxes are not equal, conservation of mass enforces motion of the phase boundary. The nitrogen fluxes are assumed to be diffusional in α-Ti and β-Ti phases, while the flux at the β-Ti / Ti$_{Liq}$ phase is assumed to be a combination diffusion and advection. The motion of the phase boundaries is given by Eqs. 5.3 and 5.4.

$$D_\alpha \frac{\partial c}{\partial r}\big|_{r=s_1^-} - D_\beta \frac{\partial c}{\partial r}\big|_{r=s_1^+} = \left[c_\beta^+ - c_\alpha^-\right]\frac{ds_1}{dt}, \qquad r = s_1 \tag{5.3}$$

$$D_\beta \frac{\partial c}{\partial r}\big|_{r=s_2^-} - k\left(c_{Ti_{Liq}}^+\right) = \left[c_{Liq}^+ - c_\beta^-\right]\frac{ds_2}{dt}, \qquad r = s_2 \tag{5.4}$$

where c_i^- [kg·m^{-3}] is the lower nitrogen concentration limit in phase i, c_i^+ [kg·m^{-3}] is the upper nitrogen concentration limit in phase i, and k [m·s^{-1}] is a mass transfer coefficient.

The Ranz-Marshall correlation is used to calculate the mass transfer coefficient, k, which is presented in Eq. 5.6.

$$Sh = 2 + 0.6\, Re^{0.5} Sc^{0.33} \tag{5.6}$$

where Sh is the Sherwood number, Re is the Reynolds number, and Sc is the Schmidt number. The Reynold's number and Schmidt number are defined as follows:

$$Re = \frac{\rho_{Liq} V_{rel} d_P}{\mu_{Liq}}, \qquad Sc = \frac{\mu_{Liq}}{\rho_{Liq} D_{Liq}} \tag{5.7}$$

where ρ_{Liq} [kg·m^{-3}] is the density of the liquid titanium, V_{rel} [m·s^{-1}] is the relative liquid velocity, d_P [m] is the sphere's diameter, and μ_{Liq} [kg·m^{-1}·s^{-1}] is the viscosity of liquid titanium. Note: the fluid velocity will be equivalent to the slip, or relative, velocity of the particle in the fluid. This is not the bulk fluid velocity as would be present in one of the commercial melt processing

technologies such as VAR or EBCHR. The mass transfer coefficient is then determined by rearranging the equation defining the Sherwood number as follows:

$$k = \frac{D_{Liq}Sh}{d_p}$$

(5.8)

5.1.2 Numerical model

Model 1 – To implement the numerical model, Eqs. 5.1 - 5.4 are linearized and solved using a finite difference numerical scheme. At the beginning of each time step Eqs. 5.1 - 5.2 determine the nitrogen concentration at each nodal point in *α-Ti* and *β-Ti* phases. Afterward, Eqs. 5.3 - 5.4 computes the displacement of the interfaces. To account for the interface motion, the nitrogen concentration in the new mesh is extrapolated from the nitrogen concentration values in the previous mesh. This occurs at all nodal points except for the nodal points at the phase boundaries where the nitrogen concentrations are constant. The solution algorithm then moves to the next time step.

Model 2 – As in the previously developed model in Chapter 4, a Landau transformation is applied to the governing equations based on a method developed by Lanam and Heckel. To simplify the numerical analysis, new positional variables, *u* and *v* are introduced for each phase boundary, with each having a range of values between 0 and 1. For the *α-Ti* phase the positional variable *r* is replaced by *u* by setting $u = \frac{r}{s_1}$, such that $0 \leq u \leq 1$. Using the chain rule, Fick's Law may be rearranged in terms of the new positional variable to yield Eq. 5.9. For the *β-Ti* phase, the positional variable *r*, is replaced by *v* by setting $v = \frac{r-s_1}{s_2-s_1}$ such that $0 \leq v \leq 1$, yielding Eq. 5.10.

$$(us_1)^{\lambda-1}\left(\frac{\partial c}{\partial t} - \left(\frac{u\frac{ds_1}{dt}}{s_1}\right)\frac{\partial c}{\partial u}\right) = \frac{\partial}{\partial u}\left(\frac{(us_1)^{\lambda-1}D_\beta}{s_1^2}\frac{\partial c}{\partial u}\right), \qquad 0 \leq u \leq 1$$

(5.9)

$$[s_1 + (s_2 - s_1)v]^2 \left(\frac{\partial c}{\partial t} + \left(\frac{(v-1)\frac{ds_1}{dt} - v\frac{ds_2}{dt}}{(s_2 - s_1)} \right) \frac{\partial c}{\partial v} \right) \qquad (5.10)$$

$$= \frac{\partial}{\partial v} \left(\frac{[s_1 + (s_2 - s_1)v]^2 D_\beta}{(s_2 - s_1)^2} \right) \frac{\partial c}{\partial v}, \qquad 0 \le v \le 1$$

Applying the chain rule, the equations that describe the phase boundary motions are written in terms of the transformed positional variables u and v, see Eqs. 5.11 and 5.12.

$$\left(\frac{D_\alpha}{s_1} \right) \frac{\partial c}{\partial u} |_{u=1} - \left(\frac{D_\beta}{(s_2 - s_1)} \right) \frac{\partial c}{\partial v} |_{v=0} = \left[c_\beta^+ - c_\alpha^- \right] \frac{ds_1}{dt} \qquad (5.11)$$

$$\left(\frac{D_\beta}{(s_2 - s_1)} \right) \frac{\partial c}{\partial v} |_{v=1} - k \left(c_{Ti_{Liq}}^+ - c_{Ti_{Liq}}^- \right) = \left[c_{Liq}^+ - c_\beta^- \right] \frac{ds_2}{dt} \qquad (5.12)$$

To implement the numerical model, Eqs. 5.9 - 5.12 are linearized using an explicit finite difference scheme. At the beginning of each time step, Eqs. 5.9 – 5.10 determine the nitrogen concentration at each nodal point in α-Ti and β-Ti phases. Afterward, Eqs. 5.11 – 5.12 are used to compute the displacement of the interfaces. To account for the interface motion, the particle is re-meshed. In contrast to the first-generation model, the nitrogen concentration in the new mesh can be taken directly from result of Eqs. 5.9 – 5.10 as the equations explicitly account for the interface motion. The solution algorithm then moves to the next time step.

Both approaches offer the opportunity to further enhance the model for both non-isothermal problems and/or problems in which varying density needs to be considered (beyond the scope of this work).

Phase boundary concentrations – the nitrogen concentration values at the phase boundaries are summarized in

Table 5-1. The data was extracted from the *Ti-N* phase diagram published by Wriedt et al. [42].

Table 5-1. Summary of the interface concentration values predicted by the titanium-nitrogen binary phase diagram for temperatures between 1700 °C and 1900 °C. The data presented for this work is extracted from a publication by Wriedt et al. [42].

Temp. [°C]	c_∞ [wt. %]	c_{Liq}^+ [wt. %]	c_β^- [wt. %]	c_β^+ [wt. %]	c_α^- [wt. %]	c_0 [wt. %]	Ref.
1700	0.00	0.04	0.16	1.75	3.60	5.00	[42]
1800	0.00	0.29	0.71	1.86	3.85	5.00	[42]
1900	0.00	0.62	1.26	1.91	4.03	5.00	[42]

Boundary and Initial Conditions – At $r = 0$, $\left(\frac{\partial c}{\partial r}\right) = 0$, and the far field nitrogen concentration in the liquid, $c_{Ti_{Liq}}^-$, is assumed to be zero, such that $c(\infty, t) = 0$.

Ti-N inclusions held at temperatures between 1700 – 1900 °C containing a uniform composition of 5 wt. % nitrogen or greater will contain only *α-Ti* phase. As the numerical models have not been formulated to predict the nucleation and formation of *β-Ti* phase, as small amount is assumed to be present at the interface with the liquid initially. Thus, for particles containing a composition of 5 wt. % nitrogen or greater, the model assumes an *α-Ti* phase throughout surrounded by a thin layer of *β-Ti* phase. The initial thickness of the *β-Ti* layer was set to be one thousand times smaller than the radius of the particle – i.e., $s_2(0) - s_1(0) = \left(\frac{d_p}{2} \times \frac{1}{1000}\right)$. The initial nitrogen concentration profile, in *β-Ti* phase, varied linearly between the phase boundary concentrations.

Analysis Domain – Each phase within the domain was discretized with a number of equally spaced nodes. For the models to function correctly, nodes must be present at each phase boundary – i.e., nodal points at $r = s_1$ and s_2 for Model 1, and $u, v = 0$ and 1 for the Model 2. A sensitivity analysis on node spacing in *α-Ti* and *β-Ti* phase regimes was conducted for both models. The results showed node spacings of 0.0010 - 0.0011 mm in *α-Ti* to be sufficient and 5 nodes, evenly spaced, to be sufficient in *β-Ti*. Further refinement showed no substantial change in the predictions.

The size of the time step used in both models did not affect the model results provided the stability criterion was met – i.e., Fo = $\frac{\Delta t \, D_i}{(\Delta r)^2} < 0.5$. However, it should be noted, that reducing the

nodal spacing forces the size of the timestep to be reduced to ensure that the stability criterion is met.

Material Properties - The diffusion coefficient for nitrogen in the allotropes of titanium has been studied by a limited number of authors [19][25]. The diffusion coefficients used by Ghazal et al. [18] are implemented in this numerical model for β-*Ti*, α-*Ti* and Ti_{Liq} phases.

$$D_\alpha = 3.1 \times 10^{-7} \exp\left(-\frac{168 \times 10^3}{RT}\right) \tag{5.13}$$

$$D_\beta = 4.6 \times 10^{-5} \exp\left(-\frac{185 \times 10^3}{RT}\right) \tag{5.14}$$

$$D_{Liq} = 1.35 \times D_{Ti} \tag{5.15}$$

In Egs. 5.13 and 5.14, R [J·K^{-1}·mol^{-1}] is the ideal gas constant and T [K] is temperature. In Eq. 5.22, D_{Liq} [m^2·s^{-1}] is the diffusion coefficient of nitrogen in liquid titanium and D_{Ti} [m^2·s^{-1}] is the self-diffusion coefficient for titanium. The self-diffusion coefficient for titanium at 1670 °C is 3.8×10^{-9} [m^2·s^{-1}] [18]. The viscosity of titanium and the density of liquid titanium used in this numerical model are 0.0052 [kg·m^{-1}·s^{-1}] and 4140 [kg·m^{-3}] [18], respectively. Unless otherwise stated, the fluid velocity or drag velocity on the particle is constant and equal to 10 mm·s^{-1}.

5.2   Results and discussion

5.2.1   Model comparison

Figure 5-3 compares the evolution in the position of the s_1 and s_2 interfaces in time using the two different model formulations. Both models predict that the β-*Ti/Ti$_{Liq}$* phase interface, s_2, will initially propagate outwards for a short period before moving inwards. This occurs as the mass flux of nitrogen outward from the particle initially exceeds the transport into the liquid leading to a build-up of nitrogen in the liquid at the *S/L* interface to the extent that it solidifies. The final dissolution times predicted are 276 s and 292 s for Model 1 and Model 2, respectively.

The shorter dissolution time predicted by Model 1 is consistent with the small amount of species mass being lost when the phase interface moves, as previously illustrated in Figure 5-1. Refining the nodal spacing in the Model 1 reduces the mass loss slightly but at the cost of

significantly increasing the execution time of the algorithm. Due to the stability criteria, halving the nodal spacing quadruples the number of timesteps required to simulate the dissolution behaviour.
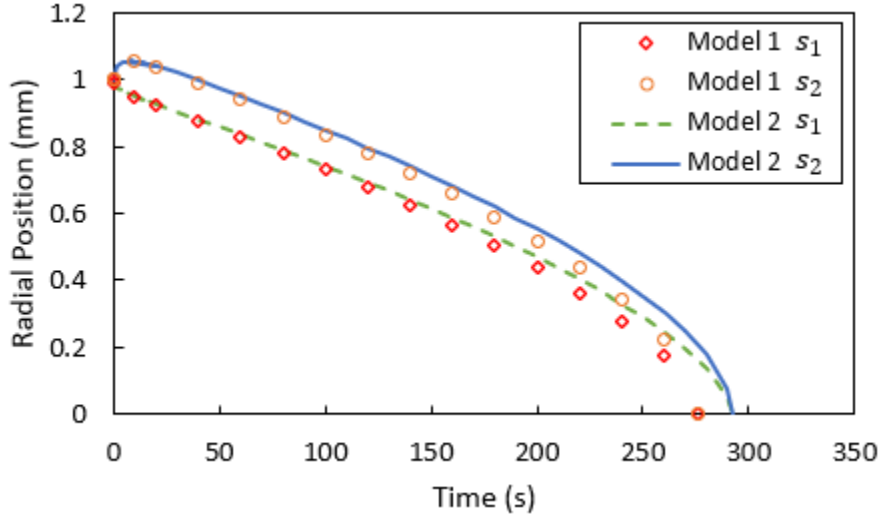
Figure 5-3. The interface positions as a function of time are presented for the first-generation numerical model and second-generation numerical model for the dissolution of a radius 1 mm *Ti-N* sphere in a CP-Ti melt pool.

Figure 5-4 compares the nitrogen concentration profiles in the particle predicted by the two models at 50, 150 and 250s. As can be seen, the extent to which the two models diverge in the predicted location of the α-*Ti*/β-*Ti* interface (indicated by the discontinuity in N wt%) increases with increasing time as the loss in species mass in Model 1 is cumulative.

To verify that Model 2 properly conserves mass, the mass of nitrogen originally contained within the particle is compared with the total amount removed from the *S/L* interface. These quantities were found to agree to within 0.8 %.

As a means of gaining some additional insight, a quantitative analysis of the nitrogen concentration gradients in the two models on either side of the α-*Ti*/β-*Ti* interface has been completed. Focusing on the predicted concentration for the nodes adjacent to the interface nodes, there is a difference between the two models on the α-*Ti* side of the interface, but not on the β-*Ti* side. The concentrations predicted for the adjacent node on the α-*Ti* side in Model 2 are 0.5-1.1% larger than the values predicted for Model 1. In Model 2, the larger nitrogen concentration values adjacent to the α-*Ti*/β-*Ti* interface in α-*Ti* phase will result in a larger gradient in concentration increasing the nitrogen flux entering the α-*Ti*/β-*Ti* interface from the α-*Ti* phase side. Given that

there is little or no difference in the flux exiting the *α-Ti*/β-*Ti* interface from *β-Ti* side, the rate of interface propagation toward the particle center would be expected to be lower for Model 2 – refer to Eq. 5.11.
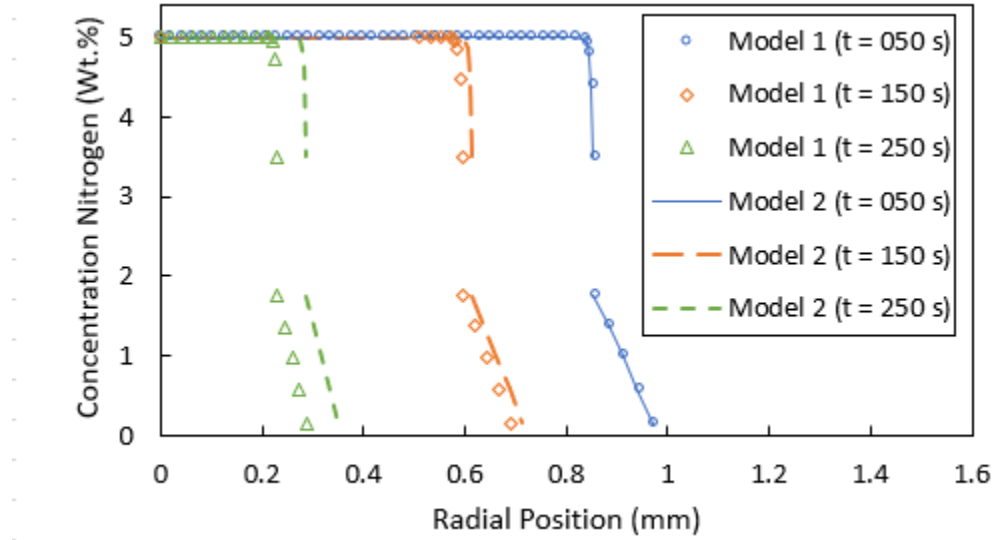
Figure 5-4. The nitrogen concentration profiles are presented for Model 1 (discrete points) and for Model 2 (continuous and dotted lines) for the dissolution of a radius 1 mm *Ti-N* sphere after immersion times of 50, 150, and 250 s in a CP-Ti melt pool.

The comparison demonstrates that both models can approximate the dissolution times of spherical *Ti-N* inclusions. However, in the formulation adopted in Model 1, inaccuracies in remapping the nitrogen concentration result in a decrease in the predicted dissolution time. For the example case shown in Figure 5-3, the dissolution times predicted with the two models are within approximately 7% of one another. For larger particles, or particles containing a larger initial wt% of N, the difference will increase.

Finally, in addition to more accurately closing the species mass balance, the formulation adopted in Model 2 is also computationally more efficient. The improved performance of the code has the potential to become important if the dissolution model is integrated into a large computation fluid dynamics (CFD) program describing one of the commercial melt refining processes.

5.2.2 Factors effecting dissolution time

In this section, an analysis is conducted to investigate the sensitivity of the dissolution time predicted by Model 2 to: material properties (nitrogen concentration limits and nitrogen diffusivities); and the melt pool conditions (temperature and fluid flow).

Material properties – A sensitivity study of the dissolution time of *Ti-N* spheres to some of the key material properties was conducted using equation 5.16.

$$Change\ in\ Dissolution\ Time\ (\%) = \frac{(DT_{BaseCase} - DT_{TestCase})}{(DT_{BaseCase})} \times 100 \qquad (5.16)$$

where DT_i is the time taken for complete dissolution of the inclusion for case *i*. *BaseCase* refers to the time for complete inclusion dissolution to occur with the material properties described in section 5.1.2 and *TestCase* refers to the case in which the parameter under consideration is varied. *Note: the parameters used in the test case simulations were varied between 25-200% of the base case values. However, in some cases the physical constraints of the system meant that the test case properties were varied over a narrower range.*

Figure 5-5 illustrates the sensitivity of the predicted dissolution time the various phase boundary concentration limits used, within the appropriate limits. The dissolution time was shown to be particularly sensitive to changes in c_{Liq}^+. Decreasing c_{Liq}^+ to 25% of the base-case value increased the dissolution time by 192.7%, while doubling c_{Liq}^+ decreased the dissolution time by 47.3 %. The dissolution time also varied with changes of c_β^-, c_β^+, and c_α^-. However, the effect was relatively small when compared with the effect of c_{Liq}^+ has on dissolution time. For example, the maximum change in dissolution times were 2.9%, 14.4% and 0.6% for changes of c_β^-, c_β^+, and c_α^-, respectively. As a reminder, the concentration limits originally adopted in the model formulation were taken from the *Ti-N* phase diagram, hence the predicted dissolution times may be altered significantly in some of the commercial Ti alloys, due to interaction effects.
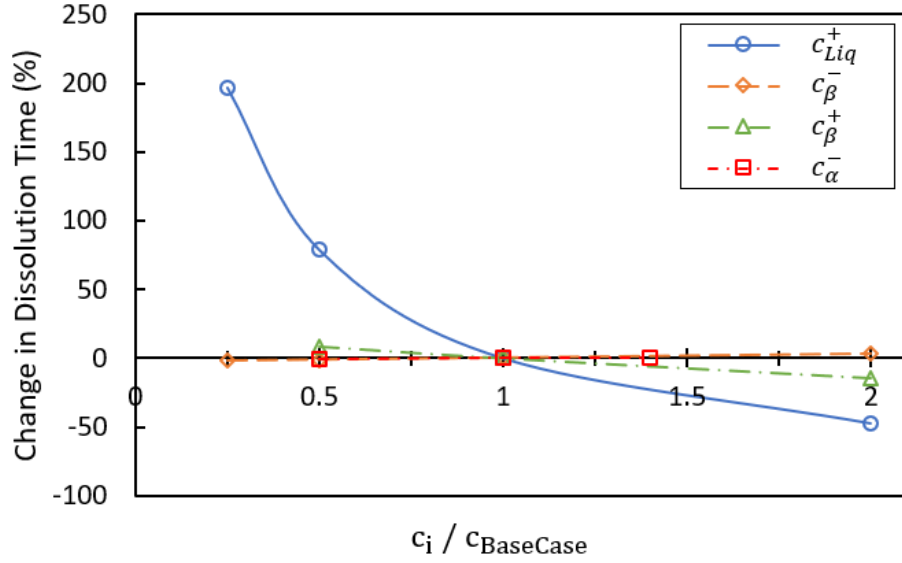
Figure 5-5. The sensitivity of dissolution time to nitrogen concentration limits in α-Ti, β-Ti, and Ti_{Liq} phases are assessed in a radius 1 mm sphere dissolving in a CP-Ti melt pool at 1700 °C.

A limited number of studies have investigated the nitrogen concentration limits in pure titanium [10][40][42]. Although the literature is far from unanimous on the exact values for c_β^-, c_β^+, and c_α^-, the results from this numerical model suggest that only approximate values are required to generate accurate predictions of dissolution time of spherical inclusions. However, an accurate value for c_{Liq}^+ for input to the numerical model is required to generate accurate dissolution times. It appears the value of c_{Liq}^+ has only been investigated in a study by Palty [40]. In the study, the melting point of CP-Ti, which affects the values of c_{Liq}^+, was 59 °C higher than the melting point currently proposed by the NSIT data base. In light of this, subsequent phase diagrams have rejected the values of c_{Liq}^+ proposed by Palty and have instead used a schematic curve between the melting point of CP-Ti and the peritectic temperature of the titanium-nitrogen system [10][42].

Figure 5-6 demonstrates that the dissolution times predicted by the model are sensitive to the nitrogen diffusion coefficients. The dissolution time was shown to be most sensitive to changes in D_{Liq}. Decreasing D_{Liq} to 25 % of the base-case value increased the dissolution time by 129.0 %, while doubling D_{Liq} decreased the dissolution time by 33.3 %. As D_{Liq} impacts the effective mass transfer coefficient utilized in the model (see Eq. 5.8), D_{Liq} directly impacts the rate at which nitrogen is removed from the solid to the liquid. In contrast changes to D_α and D_β have a much smaller effect. Doubling D_β decreased the dissolution time by 10.9 % and doubling D_α increased

the dissolution time by 3.1 %. The increase in dissolution time with an increase in D_α can be explained by considering Eq. 5.11. From Eq. 5.11, increasing D_α would decrease the rate at which the *α-Ti/β-Ti* interface propagates toward the particle center, resulting in a decrease in the amount of *β-Ti* present at a given time (which has the higher diffusion rate of the two phases), thus resulting in a longer overall dissolution time.
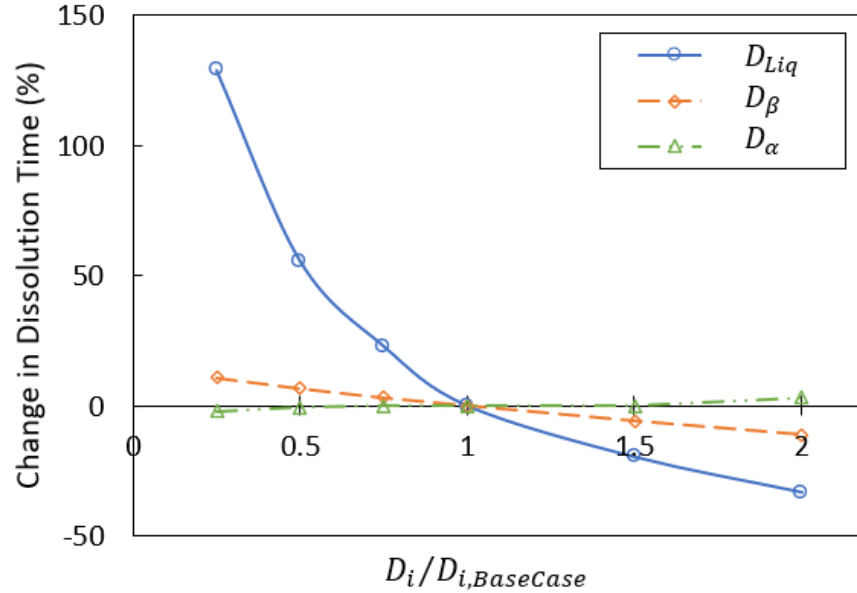
Figure 5-6. The sensitivity of dissolution time to the diffusion coefficient in *α-Ti*, *β-Ti* and Ti$_{Liq}$ phases are assessed in a radius 1 mm sphere dissolving in a CP-Ti melt pool at 1700 °C.

No experimental data on the value of D_{Liq} could be found in the literature. Lu et al. [43] noted that experimental measurement of D_{Liq} is a difficult task due to the challenge in limiting fluid motion associated with temperature induced changes in density. The value of D_{Liq} used in this model was determined via a theoretical approach. Given the sensitivity of the model and lack of experimental data on the value of D_{Liq}, caution should be observed when modelling the dissolution times for *Ti-N* inclusions. Alternatively, predictions would benefit from a more direct measurement of the mass transfer coefficient in the actual system.

Industrial melt processes - Figure 5-7 and Figure 5-8 illustrate the sensitivity of the predicted dissolution time to particle size, relative velocity and temperature. The relative velocity and temperature may be expected to be dependent on the type of melt refining operation under

investigation; for example, VAR or EBCHM. Figure 5-7 and Figure 5-8 plot the variation in time taken for complete dissolution for three particle sizes, r=0.5, 1 and 2mm.

From the results shown in both Figure 5-7 and Figure 5-8, the dissolution time is a strong function of particle radius. This is to be expected as the amount of nitrogen that must be transported from the solid to the liquid is proportional to the particle volume, which will vary with the radius cubed.

Turning to the effect of slip velocity, doubling the velocity from 10 to 20 mm/s resulted in a decrease in the dissolution time from 80 s to 60 s for the 0.5 mm radius particle, from 290 s to 215 s for the 1.0 mm radius particle and from 733 s to 538 s for the 2 mm radius particle. Hence, the results are strongly dependent on slip velocity.

As can be observed from Figure 5-8, increasing the temperature from 1700 to 1750°C resulted in a decrease in the dissolution time from 80 s to 33 s for the 0.5 mm radius particle, from 290 s to 121 s for the 1.0 mm radius particle and from 731 s to 300 s for the 2 mm radius particle. Also shown, there is a decrease in sensitivity to melt temperature with increasing temperature.

The model results presented in Figure 5-7 and Figure 5-8 point to several processing strategies that may be employed to further guarantee the elimination of *Ti-N* inclusion from material destined for safety-critical applications. These include: 1) ensuring that any particles that do make it into melt feedstocks are small; 2) ensuring that the process is operating, where feasible, at higher liquid metal temperatures; 3) ensuring that the process is operating under conditions where the liquid metal residence times are in excess of the dissolution times for the anticipated range in particle sizes and chemistries; and 4) ensuring bulk flow patterns, where possible, are optimized to yield higher particle slip velocities.
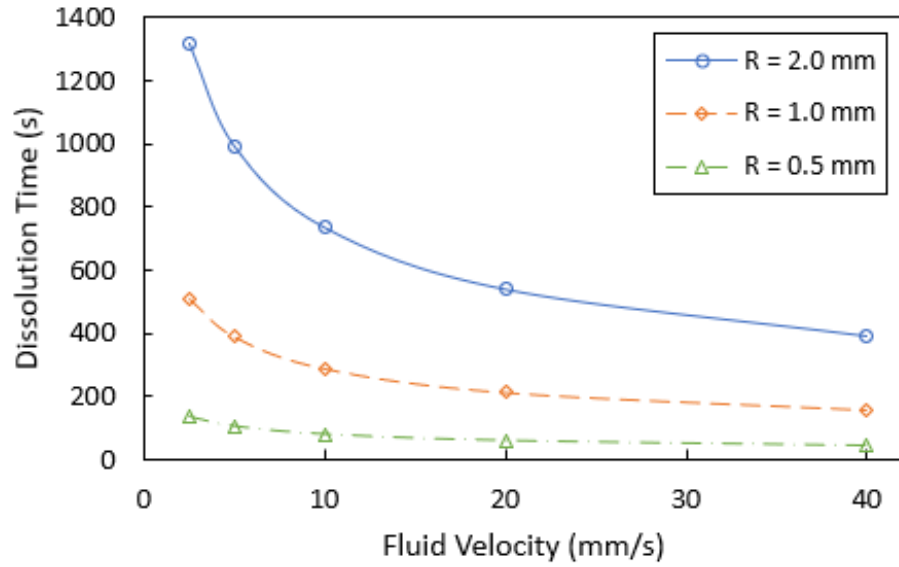
Figure 5-7. The dissolution time as a function of fluid velocity for *Ti-N* spheres of 0.5, 1 and 2mm radius in a CP-Ti melt pool at 1700 °C.
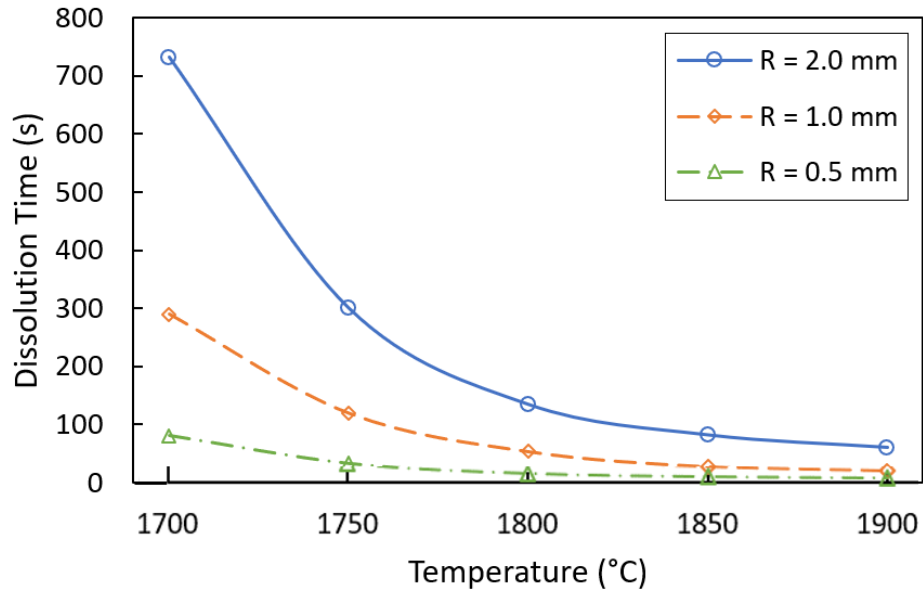

Figure 5-8. The dissolution time as a function of temperature for *Ti-N* spheres of 0.5, 1 and 2mm radius in a CP-Ti melt pool with a particle slip velocity of 10 mm·s^{-1}.

Chapter 6 Summary and Conclusions

Motivated by reducing the occurrence of HIDs in rotary grade titanium, this study developed a numerical model, based on a Landau transformation, to describe the dissolution of *Ti-N* inclusions in liquid titanium. As a prelude to the dissolution model, a numerical model of the nitriding of CP titanium was also developed.

Chapter 4 presented a novel numerical model that offers the potential to approximate the diffusive transport of nitrogen in titanium, which includes the transient displacement of the β-*Ti*/α-*Ti* and α-*Ti*/*TiN* phase boundaries, as would result from a solid at elevated temperature being subjected to a nitriding or de-nitriding atmosphere. The numerical model is based on the finite difference method and adopts a Landau transformation of the coordinates to facilitate the accurate tracking of the phase boundaries.

To verify the model formulation, the model was first applied to a semi-infinite plate geometry and compared to the predictions of an analytical model for a semi-infinite plate. The model was then applied to a finite cylindrical geometry and compared to experimentally derived data. The model results were shown to be sensitive to systematic perturbation of the diffusion coefficients, for nitrogen in β-*Ti*, α-*Ti* and *TiN* phases. Based on the sensitivity analysis, diffusion coefficients at 1650 °C of 4.3×10^{-11} m^{2}s^{-1}, 1.6×10^{-11} m^{2}s^{-1} and 1.7×10^{-12} m^{2}s^{-1} for β-*Ti*, α-*Ti* and *TiN* phases, respectively, were back calculated using the model. The phase boundary displacement and nitrogen concentration profile predicted by the model, using the diffusion coefficients outlined, closely match the experimentally derived data.

Chapter 5 presented the development of an improved numerical model for describing the dissolution of *Ti-N* particles in liquid Ti. The method accounts for the transient displacement of the α-*Ti*/β-*Ti* and β-*Ti*/Ti$_{\text{Liq}}$ phase boundaries and formulated based on the numerical model framework presented in Chapter 4. The improved approach accurately accounts for conservation of nitrogen associated with interface motion and hence has the potential to predict particle dissolution times more accurately in commercial melt refining operations. The model describes the diffusive transport of nitrogen in α-*Ti* and β-*Ti* phases, and approximates the convective transport of nitrogen at the β-*Ti*/Ti$_{Liq}$ phase boundary using the Ranz-Marshall correlation.

The results of the improved methodology (referred to as Model 2) have been compared to a second finite-difference based model formulated using the conventional approach for interface

motion (referred to as Model 1). The difference in the two formulations was assessed by considering the example case of a 1 mm radius particle in CP-Ti melt at 1700ºC. Model 1, using the conventional approach, predicted a dissolution time of 276 s whereas as Model 2, using the improved interface tracking methodology, predicted a dissolution time of 292 s. The lower dissolution time predicted by Model 1 is consistent with small amounts of mass being lost during the imprecise remapping of nitrogen concentration after the interface has moved. Model 2 can more accurately conserve nitrogen mass, and hence predicted a longer dissolution time.

Based on the results of a sensitivity analysis, Model 2 was shown to be sensitive to the diffusion coefficient in liquid Ti, D_{Liq}, and the upper nitrogen concentration limit in liquid titanium, c_{Liq}^+. Hence the overall accuracy of the model will depend on having obtained accurate estimates for the diffusion coefficient of nitrogen and solubility limit of nitrogen in the liquid alloy under investigation.

In addition to particle size, the dissolution times of spherical *Ti-N* inclusions were found to be sensitive to the particle slip velocity and the temperature of the surrounding melt pool. In practice, the residence time, thermal field and flow field that *Ti-N* particles will experience will depend on their trajectories and will vary from process to process and within a given process due to varying operating conditions.

6.1   **Future work**

It is acknowledged that this work has limitations in terms of the lack of experimental work to verify the accuracy of the numerical models, and the application of the numerical model to simulate industrial melt refining processes. Further work is recommended in the following areas:

1. The results presented in Chapter 4 indicate that the model can accurately approximate the diffusive transport of nitrogen in the *Ti-N* system at 1650 °C. However, additional experimental data over a broader range of temperatures, should be conducted to build confidence in the model's validity and to also provide additional important nitrogen diffusivity data at elevated temperatures. In conjunction with experimental measurement, the analytical solution presented in Chapter 4 offers the opportunity to estimate temperature dependent diffusion coefficients.

2. The dissolution of synthetic inclusions in liquid titanium (inclusions with non-porous structures and evenly distributed nitrogen composition) modelled in Chapter 5 is not

representative of *Ti-N* inclusions that originate from nitrided titanium sponge particles. Inclusions that originate from nitrided titanium sponge particles have a porous structure and unevenly distributed nitrogen composition. To obtain a more comprehensive understanding of *Ti-N* inclusion removal, experiments and modeling work should be conducted to better understand the dissolution of nitrided titanium sponge particles.

3. For industrial application, the numerical model describing the dissolution of synthetic inclusions should be coupled with a trajectory model (a trajectory model refers to a model which describes the motion of inclusions during melt refining processes) to describe the dissolution of inclusions during CHM and VAR processing.

Bibliography

[1]   G. Lutjering and J. Williams, *Titanium, Engineering Materials and Processes*, vol. 1, no. ASM International, 2003.

[2]   R. R. Boyer, "Properties, Compositions, and Applications of Selected Titanium Alloys | Metals Handbook Desk Edition, 2nd Ed. | Handbooks | ASM International," *ASM International*, 1998. https://dl-asminternational-org.eu1.proxy.openathens.net/handbooks/book/49/chapter/599899/Properties-Compositions-and-Applications-of (accessed Jun. 16, 2021).

[3]   M. A. Imam and F. H. Froes, "Low cost titanium and developing applications," *Jom*, vol. 62, no. 5. pp. 17–20, 2010, doi: 10.1007/s11837-010-0069-8.

[4]   I. Inagaki, T. Takechi, Y. Shirai, and N. Ariyasu, "Application and features of titanium for the aerospace industry," *Nippon Steel Sumitomo Met. Tech. Rep.*, vol. 106, no. 106, pp. 22–27, 2014.

[5]   "Titanium USA 2018," in *34Th Annual International Conference and Exhibition*, 2018, pp. 1–40, [Online]. Available: https://cdn.ymaws.com/titanium.org/resource/resmgr/02_jens_folder/titanium_usa_2018_executive_.pdf.

[6]   Fritz Appel, Jonathan David Heaton Paul, and Michael Oehring, *Gamma Titianium Aluminide Alloys*. 2011.

[7]   R. E. Shuster, "MODELING OF ALUMINUM EVAPORATION DURING ELECTRON BEAM COLD HEARTH MELTING OF TITANIUM ALLOY INGOTS," University of British Columbia, 2013.

[8]   A. Mitchell, "Electron beam melting and refining of titanium alloys," *Mater. Sci. Eng. A*, vol. 263, no. 2, pp. 217–223, 1999, doi: 10.1016/S0921-5093(98)01177-0.

[9]   J. L. Henry, S. D. Hill, J. L. Schaller, and T. T. Campbell, "Nitride inclusions in titanium ingots: A study of possible sources in the production of magnesium-reduced sponge," *Metall. Trans.*, vol. 4, no. 8, pp. 1859–1864, 1973, doi: 10.1007/BF02665413.

[10]   W. Lengauer, "The Titanium-Nitrogen System: a Study of Phase Reactions in the Subnitride Region By Means of Diffusion Couples," *Chem. Mater.*, vol. 39, no. 12, pp. 2985–2996, 1991.

[11]   F. Schwartz, "Technical Report," 1993.

[12]   R. G. Reddy, "Measurement of dissolution rates of TiN in Ti-6Al-4V," in *EBMR-State of the Art*, 1988, pp. 119–127.

[13]   W. Buttrill and C. Shamblen, "Dissolution of nitrided titanium in liquid titanium alloys," in *Titanium '95*, 1995, p. 1446.

[14]   J. P. Bellot, B. Foster, S. Hans, E. Hess, D. Ablitzer, and A. Mitchell, "Dissolution of Hard-

Alpha Inclusions in Liquid Titanium Alloys," *Metall. Mater. Trans. B Process Metall. Mater. Process. Sci.*, vol. 28, no. 6, pp. 1001–1010, 1997, doi: 10.1007/s11663-997-0054-y.

[15]   H. Mizukami, T. Kitaura, and Y. Shirai, "Nitriding Behavior of Titanium Sponge Studied using Nitrogen Gas and Dissolution Behavior of a Titanium Nitride Sponge in Titanium Alloy Melt," vol. 59, no. 1, pp. 104–112, 2019.

[16]   B. P. Bewlay and M. F. X. Gigliotti, "Dissolution rate measurements of TiN in Ti-6242," *Acta Mater.*, vol. 45, no. 1, pp. 357–370, 1997, doi: 10.1016/S1359-6454(96)00098-5.

[17]   J. A. Van Den Avyle, J. A. Brooks, and A. C. Powell, "Reducing defects in remelting processes for high-performance alloys," *Jom*, vol. 50, no. 3, pp. 22–25, 1998, doi: 10.1007/s11837-998-0374-7.

[18]   G. Ghazal, A. Jardy, P. Chapelle, and Y. Millet, "On the dissolution of nitrided titanium defects during vacuum arc remelting of Ti alloys," *Metall. Mater. Trans. B Process Metall. Mater. Process. Sci.*, vol. 41, no. 3, pp. 646–659, 2010, doi: 10.1007/s11663-009-9339-7.

[19]   H. L'Enfant, P. Laurens, M. C. Sainte Catherine, T. Dubois, and J. Amouroux, "Kinetics of titanium nitriding under CW CO2 laser radiation," *Surf. Coat. Technol.*, vol. 96, p. 80, 1998.

[20]   T. C. Illingworth and I. O. Golosnoy, "Numerical solutions of diffusion-controlled moving boundary problems which conserve solute," *J. Comput. Phys.*, vol. 209, no. 1, pp. 207–225, 2005, doi: 10.1016/j.jcp.2005.02.031.

[21]   J. Caldwell and Y. Y. Kwan, "Numerical methods for one-dimensional Stefan problems," *Commun. Numer. Methods Eng.*, vol. 20, no. 7, pp. 535–545, 2004, doi: 10.1002/cnm.691.

[22]   J. P. Bellot, E. Hess, and D. Ablitzer, "Aluminum volatilization and inclusion removal in the electron beam cold hearth melting of Ti allpys," *Metall. Mater. Trans. B Process Metall. Mater. Process. Sci.*, vol. 31, no. 4, pp. 845–854, 2000, doi: 10.1007/s11663-000-0121-0.

[23]   A. Powell, J. Van Den Avyle, and U. Pal, "Optimal Beam Pattern to Maximize Inclusion Residence Time in an Electron Beam Melting Hearth," 1997.

[24]   R. D. Lanam and R. W. Heckel, "A study of the effect of an intermediate phase on the dissolution and homogenization characteristics of binary alloys," *Metall. Mater. Trans. B*, vol. 2, no. 8, pp. 2255–2266, 1971, doi: 10.1007/BF02917558.

[25]   J. P. Bars, E. Etchessahar, and J. Debuigne, "ETUDE CINETIQUE, DIFFUSIONNELLE ET MORPHLOIQUE DE LA NITRURATION DU TITANE PAR L'AZOTE A HAUTE TEMPERATURE: PROPRIETES MECANIQUES ET STRUCTURALES DES SOLUTIONS SOLIDES Ti ALPHA-AZOTE," *J. Less Common Met.*, vol. 52, pp. 51–76, 1977.

[26]   J. Xu, C. D. Lane, J. Ou, S. L. Cockcroft, D. M. Maijer, and A. Akhtar, "Diffusion of Nitrogen

in Solid CP-Titanium at Elevated Temperature and Its Affects," *J. Mater. Res. Technol.*, pp. 1–28, 2021.

[27] W. D. Callister, *Materials science and engineering : an introduction*, vol. 52, no. 8th. 2002.

[28] L. S. Castleman, "An Analytical Approach to the Diffusion Bonding Problem," *Nucl. Sci. Eng.*, vol. 4, no. 2, pp. 209–226, 1958, doi: 10.13182/nse58-a15363.

[29] Y. Zhou and T. H. North, "Kinetic modelling of diffusion-controlled, two-phase moving interface problems," *Model. Simul. Mater. Sci. Eng.*, vol. 1, no. 4, pp. 505–516, 1993, doi: 10.1088/0965-0393/1/4/012.

[30] V. R. Voller, "An implicit enthalpy solution for phase change problems: with application to a binary alloy solidification," *Appl. Math. Model.*, vol. 11, no. 2, pp. 110–116, 1987, doi: 10.1016/0307-904X(87)90154-5.

[31] H. G. Landau, "Heat conduction in a melting solid," *Q. Appl. Math.*, vol. 8, no. 1, pp. 81–94, 1950, doi: 10.1090/qam/33441.

[32] W. D. Murray and F. Landis, "Numerical and Machine Solutions of Transient Heat-Conduction Problems Involving Melting or Freezing: Part I—Method of Analysis and Sample Solutions," *J. Heat Transfer*, vol. 81, no. 2, pp. 106–112, 1959, doi: 10.1115/1.4008149.

[33] R. A. Tanzilli and R. W. Heckel, "Numerical Solutions to the Finite, Diffusion-Controlled, Two Phase, Moving Interface Problem (with Planar, Cylinderical, and Spherical Interfaces)." AIME, 1968.

[34] H. Okamoto, "N-Ti (Nitrogen-titanium)," *J. Phase Equilibria Diffus.*, vol. 34, no. 2, p. 151, 2013, doi: 10.1007/s11669-012-0153-6.

[35] W. Lengauer, "Properties of bulk δ-TiN1-x prepared by nitrogen diffusion into titanium metal," *J. Alloys Compd.*, vol. 186, no. 2, pp. 293–307, 1992, doi: 10.1016/0925-8388(92)90016-3.

[36] I. Khidirov, "Revision of the Ti-N phase diagram as probed by neutron diffraction," *Russ. J. Inorg. Chem.*, vol. 56, no. 2, pp. 298–303, 2011, doi: 10.1134/S0036023611020100.

[37] F. W. Wood, A. Metallurgy, and O. G. Paasche, "DUBIOUS DETAILS OF NITROGEN DIFFUSION IN NITRIDED TITANIUM," vol. 40, pp. 131–137, 1977.

[38] V. S. Eremeev, Y. M. Ivanov, A. S. Panov, and I. Akad, "Diffusion coefficients of nitrogen in CP titanium," in *Proceedings of the USSR Academy of Sciences*, 1969, vol. 4, p. 262.

[39] V. D. Repkin, V. Kirkutov, G. Bespalov, and A. A. Kornilov, "Nitrogen Diffusion in Titanium," *Met. Protessy Khimii Metal.*, p. 320, 1971.

[40] A. E. Palty, H. Margolin, and J. P. Nielsen, "Titanium-Nitrogen and Titanium Boron Systems," *Trans. ASM*, vol. 46, pp. 312–328, 1954.

[41] L. E. Toth, "Transition Metal Carbides and Nitrides," *Refract. Mater.*, vol. 7, p. 1971, 1971.

[42] H. A. Wriedt and J. L. Murray, "The N-Ti (Nitrogen-Titanium) system," *Bull. Alloy Phase Diagrams*, vol. 8, no. 4, pp. 378–388, 1987, doi: 10.1007/BF02869274.

[43] H. M. Lu, G. Li, Y. F. Zhu, and Q. Jiang, "Temperature dependence of self-diffusion coefficient in several liquid metals," *J. Non. Cryst. Solids*, vol. 352, no. 26–27, pp. 2797–2800, 2006, doi: 10.1016/j.jnoncrysol.2006.03.049.